Alma Mater Studiorum · University of Bologna

School of Science
Department of Physics and Astronomy
Master Degree in Physics

Full Simulation of The Muon System of IDEA Detector Concept for Future Circular Lepton Colliders

Supervisor:
Prof./Dr. Sylvie Braibant

Co-supervisors:

Dr. Paolo Giacomelli

Prof./Dr. Isabella Garzia

Submitted by:
Mahmoud Abd Elhay Afifi Ali

Academic Year 2022/2023

Abstract

In this master thesis, a comprehensive simulation of the muon system and pre-shower subdetectors for the IDEA (International Detector for Electron-Positron Accelerator) detector concept at the Future Circular Collider electron-positron (FCC-ee) project hosted at CERN is presented. The primary objective of this work is the development of a full simulation using the GEANT4 and DD4HEP software packages for the muon detection system within the IDEA experimental apparatus, proposed for experiments at FCC-ee.

The muon detector consists of a central cylindrical barrel, bookended by two endcaps, and is envisioned to be constructed using a vast mosaic of µRWELL detectors, each with dimensions of approximately 50x50 cm^2. This thesis introduces the geometric configuration, materials, and specifications of the µRWELL detectors. The detailed simulation encompasses the interaction of ionizing particles with the detector and the subsequent digitization of electronic signals.

This research contributes valuable insights into the performance and capabilities of the proposed muon detection system, essential for the successful realization of high-precision experiments at the FCC-ee facility.

Acknowledgments

I extend my heartfelt gratitude to my esteemed supervisors, Prof./Dr. Sylvie Braibant, Dr. Paolo Giacomelli, and Prof./Dr. Isabella Garzia, for their unwavering support, guidance, and invaluable mentorship throughout my journey in this thesis work. Furthermore, I would like to express my appreciation for providing me with the opportunity to be part of such an intellectually stimulating and collaborative research group.

To my CERN supervisors, Dr. Brieuc Francois and Dr. Gerardo Ganis for their guidance and support through my internship time at CERN.

To my parents, who did their best for me to get the proper education they had not gotten themselves because of their underprivileged conditions. Here this Master's degree in nuclear physics is for you, it is a testament to your sacrifices. Your encouragement and love have been my constant motivation. And I hope to make you proud every step of the way.

To my mathematics genius teacher, Mr. Ahmed Eltoukhy, whose profound knowledge and scientific influence have not only shaped my academic journey but also ignited my passion for learning and research. Your belief in me and your invaluable mentorship have been instrumental in bringing me to where I stand today.

Finally, I want to express my deepest gratitude to Manar, my best friend and my wife, who is always by my side.

With sincere appreciation,
Mahmoud.

Contents

List of Figures

List of Tables

Chapter 1

Future Circular Collider

The Future Circular Collider (FCC)[1] investigation delves into the viability of advanced colliders accommodated within an extensive tunnel spanning around 100 kilometers in circumference. With the confirmation of the Higgs boson's existence at the LHC making a completion of the matrix of particles and interactions, which represents an essential step in advancing our understanding of fundamental physics. This matrix has formed the foundation of the "Standard Model" for many decades. The Standard Model, a coherent and predictive theory, has exhibited remarkable success in explaining all observable phenomena within the reach of collider experiments. However, alongside these achievements, the existence of certain experimental observations necessitates an expansion of the Standard Model. To account for these phenomena, comprehensive explanations are required, giving rise to a fresh set of perplexing inquiries. These challenges demand the creation of high-energy and high-intensity colliders. The FCC study establishes the groundwork for a novel research infrastructure capable of succeeding the HL-LHC and providing support to the global physics community throughout the 21st century. A race is now underway to explore realms of physics that extend beyond the confines of the Standard Model.

FCC-ee will serve as a comprehensive precision apparatus, designed to facilitate the ongoing, meticulous investigation of the fundamental aspects of nature at its tiniest scales. Its primary optimization lies in the meticulous examination of Z, W, Higgs, and top particles, enabling the scrutiny of extensive samples, including 5×10^{12} Z bosons, 10^8 W boson pairs, 10^6 Higgs bosons, and 10^6 top quark pairs.

The FCC-ee introduces an unprecedented level of sensitivity, allowing for the detection of potential indications of new physics. These signs could manifest as subtle deviations from the predictions of the Standard Model, the observation of previously forbidden decay processes, or the production of new particles characterized by exceedingly small coupling strengths. The implementation of this collider will take place in stages, progressively spanning the entire energy range, commencing from the Z pole, extending through the WW threshold, the HZ production peak, and ultimately reaching the $t\bar{t}$ threshold and beyond.

1.1 Machine overview

1.1.1 Accelerator

The accelerator design of the FCC-ee achieves high luminosity at multiple collision energies ranging from 88 to 365 GeV, all while adhering to rigorous constraints. To enable $t\bar{t}$ operation at a collision energy of 365 GeV, the cost-effective circumference of the accelerator is approximately 100 km[2]. The FCC-ee employs a double-ring collider configuration, akin to the KEKB and PEP-II B factories, which allows for a substantial number of bunches as illustrated in figure 1.1. Two beam lines intersect at four interaction points (IPs), characterized by a horizontal crossing angle of 30 mrad. Beam current varies significantly across the energy spectrum, and adjustments are primarily made by modifying the number of bunches.

In contrast to conventional electron storage rings, where equilibrium beam parameters are predominantly influenced by synchrotron radiation generated in the collider arc dipoles, the FCC-ee experiences additional effects due to beamstrahlung. Beamstrahlung, a specialized form of synchrotron radiation, arises during collisions as a result of the opposing bunch's electromagnetic field.

A top-up injection scheme is implemented to maintain the stored beam current and luminosity at their peak levels throughout the physics run. Without the top-up injection, the integrated luminosity would be significantly lower, by over an order of magnitude. Therefore, the installation of a booster synchrotron within the collider tunnel is essential.

The injection into the top-up booster occurs at 20 GeV, a process reminiscent of the injection into LEP. For the FCC-ee, it comprises a 6 GeV normal-conducting S-band linac, a prebooster (potentially the SPS) responsible for accelerating electron and positron beams from 6 to 20 GeV, a positron source where 4.46 GeV electrons from the linac collide with a hybrid target featuring a flux concentrator, and a compact positron damping ring. The linac accelerates 1 or 2 bunches per pulse, with a repetition rate of either 100 or 200 Hz. Achieving full bunch filling for Z boson running poses the most demanding requirements in terms of the number of bunches, bunch intensity, and injector flux. This entails a linac bunch intensity of 2×10^{10} particles for both electron and positron species. Alternative injector scenarios may involve a longer 20 GeV linac without a pre-booster or a recirculating superconducting linac.

1.1.2 Performance

As a result of the resurging global interest in e^+e^- physics and its corresponding discovery potential, particularly following the observation of the Higgs boson at the LHC, the FCC is not the sole contender in this pursuit. Currently, four e^+e^- collider designs are under consideration for meticulously investigating the characteristics of the Higgs boson and other standard model (SM) particles with unprecedented precision. These designs include

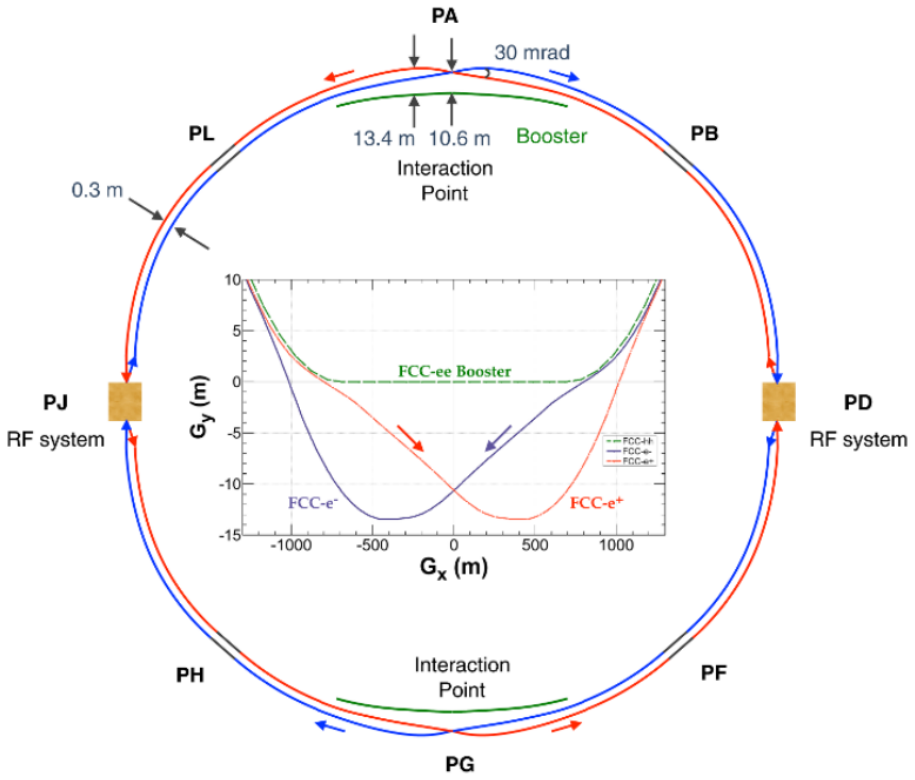

Figure 1.1: The overall layout of the FCC-ee, with a detailed view of particle trajectories near interaction point G, is illustrated. The FCC-ee rings are strategically positioned, 1 meter outside the footprint of the FCC-hh collider, which is denoted in green within the figure. Within the arc section, the e^+ and e^- rings maintain a horizontal separation of 30 cm. The primary booster ring closely follows the trajectory of the FCC-hh collider ring. Notably, the interaction points are displaced by 10.6 meters outward from the FCC-hh layout. Additionally, to mitigate synchrotron radiation effects at the interaction point, the incoming beam trajectories are adjusted to be more linear compared to the outgoing trajectories, as shown on the (G_x, G_y) plot in the middle of the figure.

two circular colliders:

- The previously described future e^+e^- Circular Collider (FCC-ee), located in a new ∼100 km tunnel at CERN.
- The Circular Electron Positron Collider (CEPC)[3], situated in a 100 km tunnel in China, offering center-of-mass energies ranging from 90 to 250 GeV.

And two linear colliders are also under study:

- The International Linear Collider (ILC)[4] project, with a center-of-mass energy of 250 GeV.
- The Compact Linear Collider (CLIC)[5], which has lowered its lowest center-of-mass energy point from 500 to 380 GeV.

The baseline luminosities anticipated to be achieved at the ILC, CLIC, CEPC, and FCC-ee center-of-mass energies are depicted in Figure 1.2. The expected integrated luminosities and operational phases at each energy level are illustrated in Figure 1.3. Among these, the FCC-ee stands out by delivering the highest data rates within a clean, precisely predictable environment, encompassing key energy points: the Z pole (91 GeV), the WW threshold (161 GeV), functioning as a Higgs factory (240 GeV), and around the $t\bar{t}$ threshold (340–365 GeV), at four interaction points. Moreover, owing to its capability to provide transverse polarization up to beam energies exceeding 80 GeV, the FCC-ee offers exceptional precision in center-of-mass energy calibration at the 100 keV level at the Z and W energy ranges, a distinctive attribute of circular colliders. Consequently, the FCC-ee is ideally positioned to deliver unparalleled statistical precision and experimental accuracy in measuring standard model particle properties. It also presents opportunities for the detection of rare new processes and the observation of subtle violations of well-established symmetries.

The FCC-ee accelerator must meet distinct requirements across its various operational modes. For instance, at the Z pole, the FCC-ee functions as an Ampere-class storage ring. During this mode, it operates with a high beam current but a relatively low RF voltage, approximately 0.1 GV. Conversely, in the $t\bar{t}$ mode, the beam current is significantly lower, comparable to the former LEP2, while a much higher RF voltage, exceeding 10 GV, is necessary. In both cases, a continuous supply of 100 MW RF power is imperative for maintaining the two circulating beams.

To address the diverse operational requirements of the FCC-ee collider rings and booster, three sets of RF cavities are proposed:

1. For high-intensity operations such as the Z mode and FCC-hh, 400 MHz mono-cell cavities (four per cryomodule) utilizing Nb/Cu thin-film technology at 4.5 K are employed.

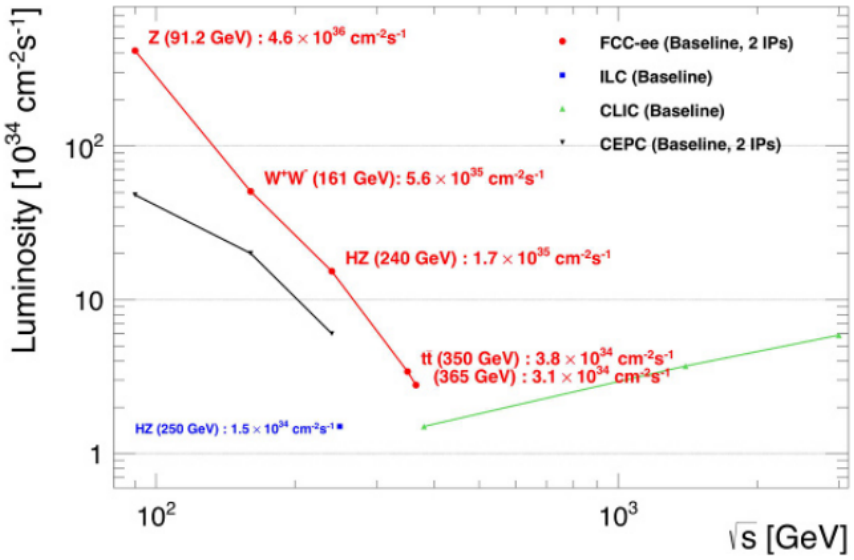

Figure 1.2: Baseline luminosities, which are the cumulative values across all interaction points, are presented as a function of the center-of-mass energy ($\sqrt{s}$) for the four prominent global e^+e^- collider initiatives: ILC (depicted as blue squares), CLIC (represented by green upward triangles), CEPC (illustrated as black downward triangles), and FCC-ee (indicated by red dots). These values are displayed with a 10% safety margin. The luminosity data for FCC-ee is sourced from this document, while the most recent CEPC parameters are estimated from[6]. The luminosity figures for the linear collider projects are referenced from[7, 8].

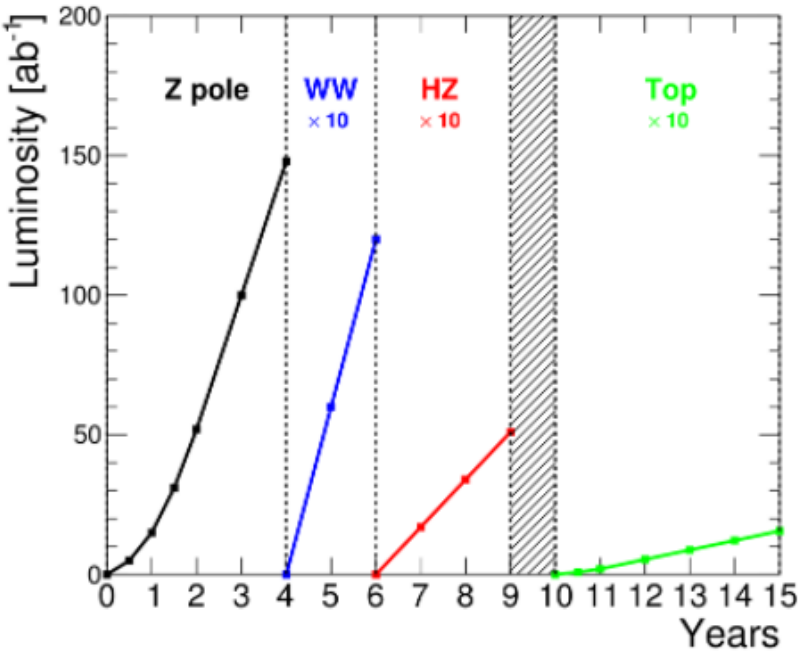

Figure 1.3: The operational plan for the FCC-ee, resulting from the five-year conceptual design study, displays the cumulative luminosity over time. It includes periods at the Z pole (black), WW threshold (blue), Higgs factory (red), and top-pair threshold (green), with hatched areas indicating necessary shutdown time for collider preparation at the highest energy levels.

2. For higher-energy modes like W, H, and $t\bar{t}$, 400 MHz four-cell cavities (four per cryomodule) based on Nb/Cu technology at 4.5 K are utilized.

3. For the $t\bar{t}$ mode, a supplementary set of 800 MHz five-cell cavities (again four per cryomodule) constructed from bulk Nb at 2 K are employed.

The installation sequence as shown in Figure 1.4 closely mirrors that of LEP, where approximately 30 cryomodules were installed per shutdown. Achieving high overall energy efficiency is accomplished through a combination of various technical and operational strategies, including the use of advanced RF power sources, innovative low-power twin-aperture magnets, and top-up injection.

1.1.3 Detector considerations

Circular colliders offer a distinct advantage by providing collisions at multiple interaction points. Consequently, various experimental collaborations are tasked with the study and

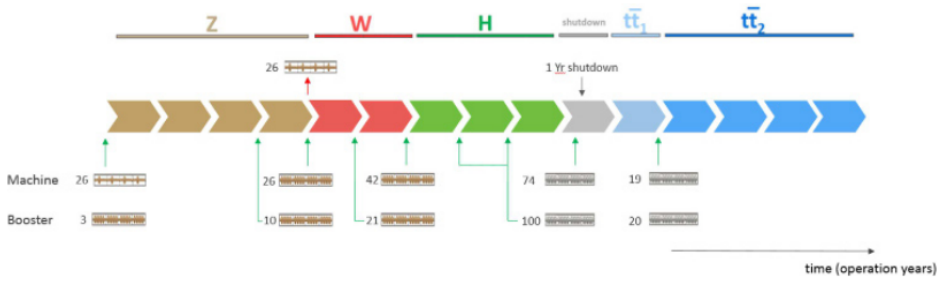

Figure 1.4: FCC-ee operational timeline, with the lower section depicting the count of cryomodules to be installed in both the collider and booster during successive winter shutdown periods; additional details are available in [9]

.

optimization of diverse detector designs tailored for the FCC-ee. These detectors must, on one hand, align their expected performance with the requirements of the physics program and statistical precision offered by the FCC-ee. This encompasses aspects such as heavy-flavor tagging, particle identification, tracking, particle-flow reconstruction, as well as lepton, jet, missing energy, and momentum & angular resolution.

On the other hand, these detectors must adhere to constraints dictated by machine performance and interaction region layout. These constraints include minimizing the impact of beam-induced background, accommodating interaction rates (which can reach up to 100 kHz at the Z pole), ensuring event size and readout speed are suitable, and limiting the detector solenoid magnetic field to 2T to prevent substantial effects on luminosity. Precise measurements of the significant center-of-mass energy spread (90 MeV at the Z pole, 500 MeV at the highest FCC-ee energies) necessitate an angular resolution better than 100 μrad for muons, and the luminometer must be situated just 1 m from the interaction point while maintaining a luminosity precision better than 10^{-4}, among other requirements.

This conceptual design report explores two general-purpose detector concepts that have been studied and optimized for the FCC-ee:

1. **CLD**[10], a well-established option based on the detector design developed for CLIC, featuring a silicon tracker and a 3D-imaging highly-granular calorimeter, enveloped by a conventional superconducting solenoid coil.

2. **IDEA**[11], an innovative and potentially more cost-effective design, incorporating a short-drift wire chamber and a dual-readout calorimeter, interspersed with a thin, lightweight superconducting solenoid coil. This choice allows for an exploration of various technology and cost considerations.

These two examples serve to demonstrate that detectors capable of meeting the stringent requirements are indeed feasible. It's important to note that while the optimization of

these two concepts will continue, other detector concepts must also be explored, as they may better align with the specific demands of the FCC-ee physics program.

1.2 Physics behind FCC-ee

Due to the resurgence of global enthusiasm for e^+e^- physics and its associated potential for groundbreaking discoveries following the observation of the Higgs boson at the LHC, the FCC finds itself amidst a shared pursuit. As the LHC data has yet to provide compelling indications of physics beyond the standard model (BSM), the landscape has markedly transformed since 2013.

The FCC-ee operates at exceptional rates within a pristine, precisely defined, and highly predictable environment. It spans a range of center-of-mass energies, including the Z pole at 91 GeV, the WW threshold at 161 GeV, serving as a Higgs factory at 240 GeV, and encompassing the $t\bar{t}$ threshold from 340 to 365 GeV, accommodating multiple interaction points. Furthermore, it provides an unprecedented level of precision in center-of-mass energy calibration, achieving accuracy down to the 100 keV level at the Z and WW energy levels. This capability stands as a unique attribute among circular colliders. A circular e^+e^- Higgs factory, denoted as LEP3, was previously proposed within the confines of the LHC tunnel in 2011[12]. In comparison to the FCC-ee, the LEP3 facility would have offered the advantage of utilizing existing infrastructure. However, this came at the significant cost of substantially reduced sensitivity to novel phenomena, manifesting in several key aspects:

(i) A luminosity diminished by a factor of 4–5 at the Z, WW, and Higgs operation points. (ii) The inability to achieve precise energy calibration at the WW threshold. (iii) The incapacity to conduct comprehensive measurements of top-quark properties. (iv) A lack of prospects for subsequent exploration of the energy frontier within the same tunnel.

Consequently, the FCC-ee stands as the optimal platform for delivering extreme statistical precision and experimental accuracy in the investigation of standard model particle properties. Additionally, it offers a gateway to the detection of rare, novel processes and presents opportunities to detect subtle deviations from established symmetries.

Historically, such precise measurements and nuanced observations have often heralded the discovery of new phenomena and particles, contributing to a deeper comprehension of fundamental physics. These historical antecedents have underscored the pivotal role of precision measurements at lower energies in guiding the development of higher-energy particle accelerators. For instance, during the latter half of the 1970s, precision measurements of neutral currents played a pivotal role in inferring the existence of the W and Z bosons, along with their mass values. These measurements, in turn, determined the dimensions of the LEP tunnel. Subsequently, the CERN SppS collider detected the W and Z bosons in the early 1980s, with their masses aligning with the earlier predic-

tions. Furthermore, the CERN LEP e^+e^- collider, in the 1990s, conducted high-precision measurements of the properties of the Z and W bosons [13, 14]. These measurements not only decisively determined the count of light, active neutrinos but also enabled the estimation of the mass of the yet-to-be-observed top quark. The top quark was subsequently discovered at the Tevatron within the predicted mass range, with the Tevatron measurement of m_{top} serving as a critical input. Consequently, the ensemble of precision measurements, including those from LEP/SLC, the Tevatron, and low-energy sources, led to a remarkably accurate prediction for the mass of the Higgs boson, observed at the LHC in 2012 within the projected mass range. Importantly, these predictions were grounded in the Standard Model, lacking any additional particle content beyond what is presently known.

With the remarkable discovery of the Higgs boson, the Standard Model appears to be a well-established theory with its predictions constrained primarily by uncertainties in theoretical calculations and input parameters. However, numerous experimental observations undeniably point to the existence of new phenomena in the universe. These include non-baryonic dark matter, the observed cosmological baryon-antibaryon asymmetry, and the presence of finite yet exceedingly small neutrino masses. These phenomena collectively indicate the presence of physics beyond the Standard Model.

The remarkable agreement between the predicted and observed masses of particles such as the W boson, top quark, and Higgs boson, coupled with the absence of significant deviations in collider experiments thus far, suggests that the energy scale of new physics or the associated coupling strengths may be exceptionally high or weak, respectively. Any new hint or discovery, whether it manifests as the observation of a new particle, an entirely unobserved phenomenon, or even a subtle deviation from Standard Model predictions, would represent a monumental breakthrough in our understanding of fundamental physics.

As a result, the next-generation accelerator project must possess the capacity for the most comprehensive and far-reaching research endeavors, and the Future Circular Collider (FCC) is positioned to fulfill this role. The FCC-ee, in particular, is poised to scrutinize the properties of the Z boson, W boson, Higgs boson, and top quark with unprecedented precision through e^+e^- collisions. This precision will enable investigations into physics at much higher energy scales or with much smaller coupling strengths. Among proposed e^+e^- colliders at the electroweak scale, the FCC-ee stands as the most potent, especially when considering the duration of its operation.

1. Precise measurements of a comprehensive set of electroweak and Higgs observables.

2. Stringent constraints on numerous parameters of the Standard Model.

3. Detection of subtle yet significant deviations from Standard Model predictions.

4. Observation of rare new processes or particles that defy Standard Model expectations.

Moreover, the FCC-ee adheres to the guideline established in the European Strategy for Particle Physics 2020, which stipulates that the accelerator should be designed for potential future upgrades. In this regard, the FCC-ee tunnel has been meticulously designed to accommodate the FCC-hh, a hadron collider boasting a remarkable center-of-mass energy of 100 TeV. The synergy between the FCC-ee and FCC-hh is poised to establish an unrivaled frontier in energy and precision in high-energy physics.

While the primary objective of the FCC-ee design study was to demonstrate the accelerator's feasibility, it has not only met but exceeded initial luminosity expectations (as depicted in Figs. 1.1 and 1.2). This success has instilled confidence in the integration of detectors at collision points and the ability to achieve beam energy calibration targets. Although the exploration of the FCC-ee's physics capabilities remains at an early stage, the subsequent sections provide a glimpse of the extraordinary scientific potential awaiting discovery.

1.2.1 Precision electroweak measurements

Since the pioneering work by Veltman[15], it has been established that electroweak quantum corrections are highly responsive to particles characterized by electroweak couplings and significantly elevated masses that are beyond the direct reach of contemporary collider experiments. Notably, the cases of the top quark and the Higgs boson are of particular interest; despite their substantial masses, their contributions do not exhibit the expected decoupling behavior. Subsequent investigations in the late 1980s revealed that these quantum corrections could be categorized into distinct blocks, each with varying degrees of sensitivity. Precise measurements of these observables thus emerge as a valuable tool for detecting the potential presence of additional particles connected to standard model interactions in a broader context. The FCC-ee, through its capacity for high-precision measurements of properties related to the Z boson, W boson, Higgs boson, and top quark, as well as fundamental input parameters like the electromagnetic and strong coupling constants at the Z mass scale, affords a unique sensitivity to the existence of new particles with masses ranging from 10 to 70 TeV.

Precision electroweak measurements at FCC-ee constitute a pivotal component of the physics program, offering a broad and highly complementary sensitivity to new physics, particularly when contrasted with measurements of Higgs boson properties. Drawing upon the experiences gained from LEP while benefiting from a substantial increase in statistical data and the enhanced prospects for beam energy calibration, we anticipate achieving a significant leap in measurement precision. This advancement is summarized in Table 1.1, which provides an overview of key quantities and experimental uncertainties in comparison to current values.

Table 1.1: Electroweak Quantity Measurements at FCC-ee[16].

Observable	Present Value	Error	FCC-ee Stat.	FCC-ee Syst.	Comment and Dominant Exp. Error
m_Z (keV)	91,186,700	2200	5	100	Beam energy calibration
Δm_Z (keV)	2,495,200	2300	8	100	Beam energy calibration
R_Z ($\times 10^3$)	20,767	25	0.06	0.2–1.0	Ratio acceptance for leptons
$\alpha_s(m_Z)$ ($\times 10^4$)	1196	30	0.1	0.4–1.6	From R_l^Z above
R_b ($\times 10^6$)	216,290	660	0.3	< 60	Stat. extrapol. from SLD
σ_0^{had} ($\times 10^3$ nb)	41,541	37	0.1	4	Peak cross-section luminosity
N_ν ($\times 10^3$)	2991	7	0.005	1	Luminosity measurement
$\sin^2\theta_{eff}^W$ ($\times 10^6$)	231,480	160	3	2–5	From $A_{\mu\mu}^{FB}$ at Z peak
$1/\alpha_{QED}(m_Z)$ ($\times 10^3$)	128,952	14	4	Small	From $A_{\mu\mu}^{FB}$ off peak
$A_{b,0}^{FB}$ ($\times 10^4$)	992	16	0.02	1–3	b-quark asymmetry at Z pole
$A_{pol,\tau}^{FB}$ ($\times 10^4$)	1498	49	0.15	< 2	τ Polarisation and charge asymmetry
m_W (MeV)	80,350	15	0.5	0.3	From WW threshold scan
Δm_W (MeV)	2085	42	1.2	0.3	From WW threshold scan
$\alpha_s(m_W)$ ($\times 10^4$)	1170	420	3	Small	From R_l^W
N_ν ($\times 10^3$)	2920	50	0.8	Small	Ratio of invis. to leptonic in radiative Z returns
m_{top} (MeV)	172,740	500	17	Small	From $t\bar{t}$ threshold scan
Δm_{top} (MeV)	1410	190	45	Small	From $t\bar{t}$ threshold scan
$\lambda_{top}/\lambda_{SM}^{top}$	1.2	0.3	0.1	Small	From $t\bar{t}Z$ couplings $\pm 30\%$

Moreover, FCC-ee's remarkable statistical capabilities enable ancillary measurements of input parameters essential for precision electroweak calculations. Notably, these encompass determining the top quark mass (m_{top}) through a thorough exploration of the $t\bar{t}$ production threshold, as well as the direct assessment of the QED running coupling constant (α_{QED}) at the Z boson mass (m_Z) via Z-γ interference. Additionally, the strong coupling constant (α_S) can be scrutinized through measurements of branching fractions within the Z, W, and τ lepton channels, comparing the hadronic and leptonic outcomes.

The significance of these supplementary measurements is underscored by the current state of the Standard Model's fit to precision data available to date[17]. Presently, Standard Model predictions and their associated uncertainties regarding the W boson mass (m_W) and the effective weak mixing angle ($\sin^2\theta_{\text{eff}}$), which stand as follows.

$$\begin{aligned} m_W &= (80.3584 \pm 0.0055_{m_{\text{top}}} \\ &\quad \pm 0.0025_{m_Z} \pm 0.0018_{\alpha_{\text{QED}}} \\ &\quad \pm 0.0020_{\alpha_S} \pm 0.0001_{m_H} \\ &\quad \pm 0.0040_{\text{theory}})\,\text{GeV} \\ &= (80.358 \pm 0.008_{\text{total}})\,\text{GeV}, \\ \sin^2\theta^W_{\text{eff}} &= (0.231488 \pm 0.000029_{m_{\text{top}}} \\ &\quad \pm 0.000015_{m_Z} \pm 0.000035_{\alpha_{\text{QED}}} \\ &\quad \pm 0.000010_{\alpha_S} \pm 0.000001_{m_H} \\ &\quad \pm 0.000047_{\text{theory}}) \\ &= (0.23149 \pm 0.00007_{\text{total}}). \end{aligned}$$

These theoretical predictions was aligned with the global average of their direct measurements:

$$m_W = 80.379 \pm 0.012\,\text{GeV},$$

and

$$\sin^2\theta^W_{\text{eff}} = 0.23153 \pm 0.00016.$$

Until the new W mass determination at the Tevatron CDF experiment, which reported a deviation from the SM expectation at the 7 σ level:

$$m_W = 80.4335 \pm 0.0064(stat) \pm 0.0069(syst)\,\text{GeV}.$$

If the measurement is confirmed by other experiments, it would suggest that there is new physics beyond the Standard Model. This is an exciting possibility, as it would mean that we are on the verge of a new revolution in our understanding of the universe.

1.2.2 The Higgs Boson

Since the discovery of the Higgs boson, numerous investigations into its properties and couplings have taken place at the Large Hadron Collider (LHC), confirming the Standard Model (SM) predictions at the 10–20% precision level. Substantial improvements are expected in the coming years and during the High-Luminosity LHC (HL-LHC) phase, potentially achieving precision levels within a few percent[18]. A 5% deviation from the SM in these measurements could signal the existence of BSM physics at energy scales around 1 TeV.

The remarkable achievements and future prospects of the LHC program mark the beginning of a new era, where the Higgs boson evolves from being a subject of discovery into a powerful exploration tool. The Future Circular Collider (FCC) positions itself as the most potent successor to inherit and expand upon the Higgs physics legacy established at the LHC. On one front, it will broaden the range of measurable Higgs properties, including elusive decays, as well as the total width and self-coupling of the Higgs boson. These enhancements will enable more profound and model-independent determinations of Higgs couplings.

On another front, the FCC's combination of superior precision and energy capabilities creates a framework where indirect and direct probes of new physics seamlessly collaborate. They work together to characterize the nature of potential discoveries. Higgs boson physics, involving approximately 10^6 Higgs decays, constitutes the core of the FCC-ee experimental program. The FCC-ee will inclusively measure Higgs production, treating it as a recoil in the process $e^+e^- \to ZH$. This approach permits the absolute measurement of the Higgs coupling to the Z boson, serving as a foundation for model-independent assessments of its total width and other couplings through branching ratio measurements.

The leading Higgs couplings to SM particles (denoted as g_{HXX} for particle X) will be probed by the FCC-ee with sub-percent precision. With model-related uncertainties eliminated at the FCC-ee, a fully complementary research program will be conducted at the FCC-hh and FCC-eh colliders to complete the comprehensive picture of Higgs boson properties. This endeavor encompasses precise measurements of rare Higgs decays (e.g., $H \to \gamma\gamma$, $H \to \mu\mu$, $H \to Z\gamma$), the identification of invisible decays ($H \to 4\nu$), and the determination of the g_{Htt} coupling with percent-level precision.

Both indirect measurements at the FCC-ee and direct measurements at the FCC-hh and FCC-eh will scrutinize the Higgs self-coupling, thereby probing the characteristics of the Higgs potential.

We will emphasize the synergies among all facets of the FCC Higgs program by conducting global fits of Higgs and Electroweak (EW) parameters. Through this synergy and complementarity, the FCC emerges as the most potent facility for a comprehensive exploration of the Higgs boson and Electroweak Symmetry Breaking (EWSB).

The primary goal of the FCC-ee program is to achieve a model-independent deter-

mination of the Higgs boson's width (Γ_H) and its couplings (g_{HXX}) with an accuracy at or below one percent. This level of precision is essential to explore energy scales up to 10 TeV and potentially beyond, by examining potential deviations among various couplings. Additionally, it's important to note that higher-order corrections to Higgs couplings within the Standard Model typically reach a few percent. To rigorously investigate the quantum properties of the Higgs sector, it is imperative to precisely measure its characteristics at a level of a few per mille or better.

Attaining this level of precision necessitates the analysis of a substantial experimental dataset comprising no less than one million Higgs bosons. At e^+e^- colliders, the primary mechanisms for Higgs production are the Higgsstrahlung process ($e^+e^- \to HZ$) and WW fusion ($e^+e^- \to WW \to H\nu\bar{\nu}$). The cross-sections for these processes are depicted in Figure 1.5 as functions of the center-of-mass energy ($\sqrt{s}$). Although the total cross-section reaches its maximum at $\sqrt{s} = 260$ GeV, the event rate per unit of time is maximized at 240 GeV due to the specific luminosity profile of the circular collider. With a cross-section of 200 femtobarns (fb) at $\sqrt{s} = 240$ GeV, generating one million events requires an integrated luminosity of at least $5\,\text{ab}^{-1}$. This dataset, predominantly comprising HZ events, can be further enhanced by collecting approximately 180,000 HZ events and 45,000 WW-fusion events with an integrated luminosity of $1.5\,\text{ab}^{-1}$ at $\sqrt{s} = 365$ GeV.

At $\sqrt{s} = 240$ GeV, the determination of Higgs boson couplings follows the strategy outlined in Reference [19], with an improved analysis that leverages the enhanced performance of the CLD detector design. The total Higgs production cross-section is ascertained by counting $e^+e^- \to HZ$ events, tagged with a leptonic Z decay ($Z \to \ell^+\ell^-$), regardless of the Higgs boson's decay. An illustrative example of such an event is presented in Figure 1.6 (left). The recoil mass (m_{Recoil}) of the system recoiling against the lepton pair is precisely computed from the momenta of the leptons and the conservation of total energy-momentum: $m^2_{\text{Recoil}} = s + m_Z^2 - 2\sqrt{s}(E^+ + E^-)$. Consequently, HZ events exhibit a recoil mass (m_{Recoil}) equal to the Higgs boson mass (m_H) and can be readily identified based on the accumulation of events around this mass value. Counting these events facilitates the precise determination of the HZ cross-section (σ_{HZ}) in a model-independent manner. This high-precision cross-section measurement alone serves as a powerful tool for probing the SM predictions for the Higgs boson at the loop level. Under the assumption that the coupling structure mirrors that of the SM, this cross-section is directly proportional to the square of the Higgs boson's coupling to the Z boson, denoted as g_{HZZ}.

Building upon this powerful measurement, the Higgs boson width (Γ_H) can then be inferred by counting the number of HZ events in which the Higgs boson decays into a pair of Z bosons. Under the same coupling assumption, this number is proportional to the ratio $\sigma_{HZ} \times \mathcal{B}(H \to ZZ)/\Gamma_H$, hence to g^2_{HZZ}/Γ_H. The measurement of g_{HZZ} described above thus allows Γ_H to be extracted. The numbers of events with exclusive

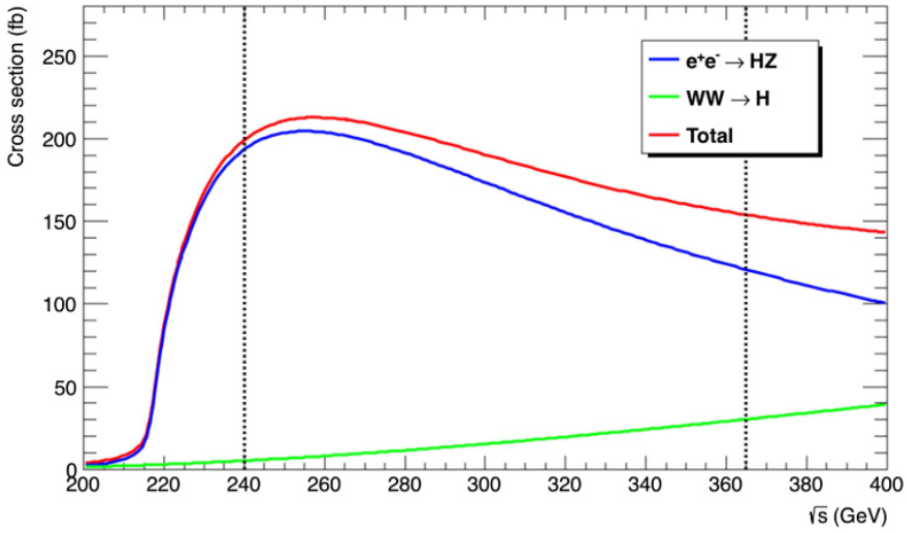

Figure 1.5: Cross section for Higgs boson production as a function of the center-of-mass energy in unpolarized electron-positron (e^+e^-) collisions. The blue and green curves represent the Higgsstrahlung and WW fusion processes, respectively, while the red curve shows the total production cross section. The vertical dashed lines on the plot indicate the selected center-of-mass energies at the FCC-ee, which are crucial for the precise measurement of the Higgs boson's properties.

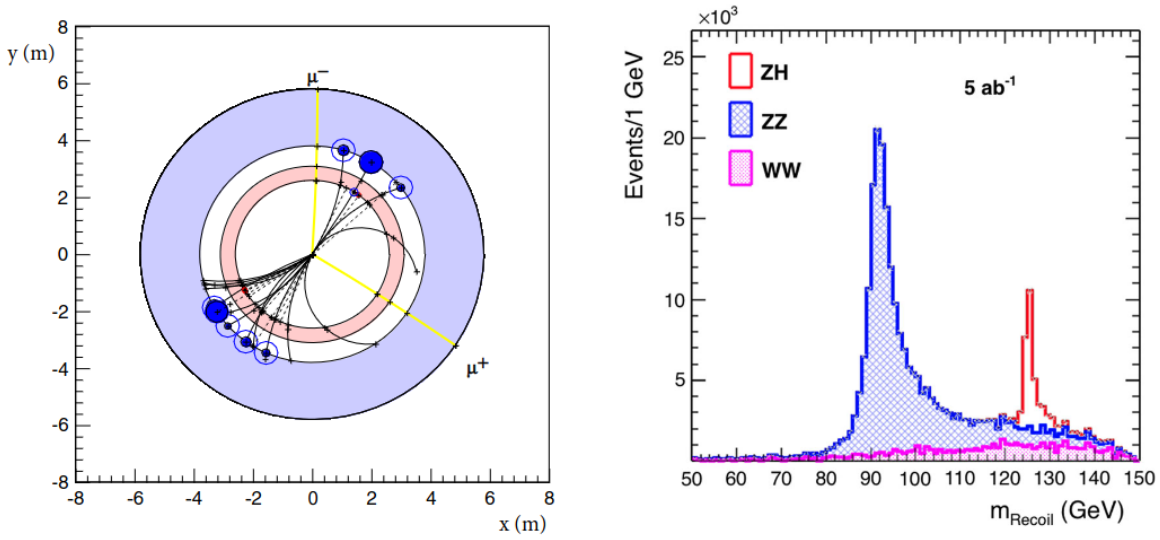

Figure 1.6: Left: Schematic transverse view of an $e^+e^- \to HZ$ event with $Z \to \mu^+\mu^-$ and the Higgs boson decaying hadronically. The two muons from the Z decay are highlighted. Right: Distribution of the recoil mass against the muon pair, determined through total energy-momentum conservation, with an integrated luminosity of 5 ab^{-1} and the CLD detector design. The peak around 125 GeV (in red) corresponds to HZ events, while the remaining distribution (in blue and pink) originates from ZZ and WW production.

decays of the Higgs boson into $b\bar{b}$, $c\bar{c}$, gg, $\tau^+\tau^-$, $\mu^+\mu^-$, W^+W^-, $\gamma\gamma$, $Z\gamma$, and invisible Higgs boson decays (tagged with the presence of just one Z boson and missing mass in the event) measure $\sigma_{HZ} \times \mathcal{B}(H \to XX)/\Gamma_H$ with precisions indicated in Table 1.2.

With σ_{HZ} and Γ_H known, the numbers of events are proportional to the square of the g_{HXX} coupling involved. In practice, the width and the couplings are determined with a global fit, which closely follows the logic of Ref.[20]. The results of this fit are summarized in Table 1.3 and are compared to the same fit applied to HL-LHC projections [18] and to those of other e^+e^- colliders exploring the 240-to-380 GeV center-of-mass energy range. Table 1.3 also shows that the extractions of Γ_H and of g_{HWW} from the global fit are significantly improved by the addition of the WW-fusion process at $\sqrt{s} = 365$ GeV, as a result of the correlation between the HZ and $\nu\bar{\nu}H$ processes.

Table 1.2: Relative statistical uncertainty on $\sigma_{HZ} \times BR(H \to XX)$ and $\sigma_{\nu\bar{\nu}H} \times BR(H \to XX)$, as expected from the FCC-ee data, obtained from a fast simulation of the CLD detector and consolidated with extrapolations from full simulations of similar linear-collider detectors (SiD and CLIC).

$\sqrt{s}$ (GeV)	240		365	
Luminosity (ab^{-1})	5		1.5	
$\delta(\sigma BR)/\sigma BR(\%)$	HZ	$\nu\bar{\nu}H$	HZ	$\nu\bar{\nu}H$
$H \to$ any	± 0.5		± 0.9	
$H \to b\bar{b}$	± 0.3	± 3.1	± 0.5	± 0.9
$H \to c\bar{c}$	± 2.2		± 6.5	± 10
$H \to gg$	± 1.9		± 3.5	± 4.5
$H \to W^+W^-$	± 1.2		± 2.6	± 3.0
$H \to ZZ$	± 4.4		± 12	± 10
$H \to \tau\tau$	± 0.9		± 1.8	± 8
$H \to \gamma\gamma$	± 9.0		± 18	± 22
$H \to \mu^+\mu^-$	± 19		± 40	
$H \to$ invisible	< 0.3		< 0.6	

In addition to the unique electroweak precision measurement program presented earlier, the FCC-ee provides the best model-independent precisions for all couplings accessible from Higgs boson decays among the e^+e^- collider projects at the electroweak (EW) scale. With larger luminosities delivered to several detectors at several center-of-mass energies ($\sqrt{s}$) of 240 GeV, 350 GeV, and 365 GeV, the FCC-ee improves on the model-dependent HL-LHC precision by an order of magnitude for all non-rare decays. This capability enables the FCC-ee to scrutinize the Higgs boson at the one-loop level of the Standard Model without the need for a costly e^+e^- center-of-mass energy upgrade. Additionally, the FCC-ee determines the Higgs boson width (Γ_H) with a remarkable precision of 1.3%, which, in turn, allows the HL-LHC measurements to be interpreted

Table 1.3: Precision determined in the κ framework for the Higgs boson couplings (κ) and total decay width (Γ), as expected from the FCC-ee data, is compared to those from HL-LHC and other e^+e^- colliders exploring the 240–380 GeV center-of-mass energy range.

Collider	**HL-LHC**	**ILC 250**	**CLIC 380**	**LEP3 240**	**CEPC 250**	**FCC-ee 240+365**	**HL-LHC**	
Lumi (ab^{-1})	3	2	1	3	5	5240 + 1.5	365 + 4	
Years	25	15	8	6	7	3 + 4		
$\delta\alpha_H/\alpha_H$ (%)	SM	3.6	4.7	3.6	2.8	2.7	1.3	1.1
$\delta g_{HZZ}/g_{HZZ}$ (%)	1.5	0.3	0.60	0.32	0.25	0.2	0.17	0.16
$\delta g_{HWW}/g_{HWW}$ (%)	1.7	1.7	1.0	1.7	1.4	1.3	0.43	0.40
$\delta g_{Hbb}/g_{Hbb}$ (%)	3.7	1.7	2.1	1.8	1.3	1.3	0.61	0.56
$\delta g_{Hcc}/g_{Hcc}$ (%)	SM	2.3	4.4	2.3	2.2	1.7	1.21	1.18
$\delta g_{Hgg}/g_{Hgg}$ (%)	2.5	2.2	2.6	2.1	1.5	1.6	1.01	0.90
$\delta g_{H\tau\tau}/g_{H\tau\tau}$ (%)	1.9	1.9	3.1	1.9	1.5	1.4	0.74	0.67
$\delta g_{H\mu\mu}/g_{H\mu\mu}$ (%)	4.3	14.1	n.a.	12	8.7	10.1	9.0	3.8
$\delta g_{H\gamma\gamma}/g_{H\gamma\gamma}$ (%)	1.8	6.4	n.a.	6.1	3.7	4.8	3.9	1.3
$\delta g_{Htt}/g_{Htt}$ (%)	3.4	–	–	–	–	–	–	3.1
$BR(E_XO)$ (%)	SM	< 1.7	< 2.1	< 1.6	< 1.2	< 1.2	< 1.0	< 1.0

in a model-independent way. Other e^+e^- colliders at the EW scale are constrained by the precision with which the HZ or the WW fusion cross sections (σ) can be measured, depending on the luminosity delivered at either 240–250 GeV, or 365–380 GeV, or both.

1.2.3 Discovery potential for new physics

More specific extensions of the standard model have been proposed to account for the observed agreement between collider experiments and Standard Model predictions, while also addressing the increasing experimental evidence supporting various new phenomena, such as non-baryonic dark matter, small neutrino masses, and the baryon asymmetry of the universe. These extensions often predict either exceedingly minor deviations from SM forecasts in electroweak precision observables (EWPO) and precise Higgs measurements, or the presence of novel, light, or heavy particles, or sometimes a combination of both. The FCC-ee presents a unique opportunity to scrutinize these extensions. In particular, it offers the capacity to investigate numerous Z boson decays that are either rare or forbidden within the SM framework, leveraging the vast dataset of approximately 5×10^{12} events produced at the Z pole. This section provides an overview of the remarkable sensitivity of the FCC-ee to a carefully chosen yet representative collection of BSM scenarios and models.

Right-handed neutrinos

Neutrino oscillations, which demonstrate the existence of neutrino mass m_ν [21], offer compelling laboratory evidence pointing beyond the realm of renormalizable interactions found within the Standard Model. Unraveling the origin of neutrino masses could pave the path towards a deeper comprehension of particle masses, as well as offer potential solutions to persistent questions in particle physics, such as the enigma surrounding the baryon asymmetry in the universe and the mystery of dark matter.

A minimal and theoretically natural explanation for the observed smallness of neutrino masses entails the existence of non-renormalizable Majorana mass terms for neutrinos. These terms may emerge through the presence of heavy right-handed neutrinos characterized by Majorana mass terms [22]. Consequently, within discussions about forthcoming scientific endeavors, the capacity to experimentally probe right-handed neutrinos (also referred to as "sterile neutrinos") has emerged as a pivotal benchmark for unlocking new discoveries. Right-handed neutrinos offer a wealth of potential signatures at the FCC-ee, spanning from their influence on precision measurements to the potential observation of their decays.

In certain scenarios, it has been proposed that the right-handed neutrino mass scale (denoted as M) could share a common origin with the electroweak scale. As the limit $M \to 0$ yields an approximate $B - L$ symmetry, it is technically plausible for M to be relatively small. Detailed examinations of how relatively light right-handed neutrinos

could address fundamental conundrums, such as the baryon asymmetry in the universe and the enigma of dark matter. These models are categorized as "inverse see-saw models" and "linear see-saw models", and they remain consistent with the concept of "minimal flavor violation". For a contemporary review of the collider implications of neutrino mass models, refer to [23].

Right-handed neutrinos exert their influence on precision measurements through their mixing with their left-handed counterparts, characterized by the mixing angle Θ. After diagonalization, this results in the emergence of heavy and light mass eigenstates. The light neutrino states, predominantly left-handed in nature, acquire a minor sterile component, leading to an apparent violation of the unitarity of the PMNS matrix [24]. This non-unitarity in the PMNS matrix manifests as systematic shifts in various observables involving neutrinos, resulting in a distinct pattern of deviations from the SM.

Among these observables, the Fermi constant G_F stands out as one of the most significant. It is measured with exceptional precision in muon decays ($\mu \to e\nu_\mu\nu_e$) and serves as an input parameter for electroweak precision observables. In the FCC-ee era, where many of these observables are expected to be measured with a precision level of 10^{-5} or better, any substantial reduction in neutrino coupling of that magnitude will become discernible. Additional observables of great precision, suitable for testing PMNS matrix (non)unitarity, encompass charged current branching ratios, especially $\tau \to \ell\nu_\tau\nu_\ell$ and $W \to \ell\nu_\ell$, rare lepton-flavor-violating processes ($\ell \to \ell'\gamma$, $\ell \to 3\ell'$), and weak cross sections for processes such as $e^+e^- \to HZ$, ZZ, and W^+W^-. For instance, with 1.5×10^{11} tau lepton pairs produced, the tau leptonic branching ratios should be measurable to a relative precision better than 10^{-5}. The sensitivity to heavy neutrinos, as derived from FCC-ee precision measurements in the (θ^2, M) plane, is indicated by the horizontal blue lines in Figure 1.7. Notably, lepton universality and the wealth of available electroweak precision observables will enable the distinct determination of the three lepton flavor mixing angles. Furthermore, the sensitivity to heavy neutrinos, as inferred from precision measurements, extends well beyond the 100 TeV scale, showcasing a scenario in BSM physics where decoupling does not apply.

Hidden sector

The compelling evidence for the existence of dark matter has spurred extensive investigations into potential particle interactions involving dark matter. Despite the limited signals in searches for conventional Weakly Interacting Massive Particle (WIMP) dark matter candidates, a shifting theoretical perspective inspired by observable sector characteristics suggests that the dark sector could be more intricate than initially anticipated. Notably, the Higgs and Z-boson, as the sole massive neutral bosons in the Standard Model (SM), represent promising candidates for exploring the dark sector. They may readily decay into new, light neutral fields beyond the SM, offering a unique window into this hidden realm.

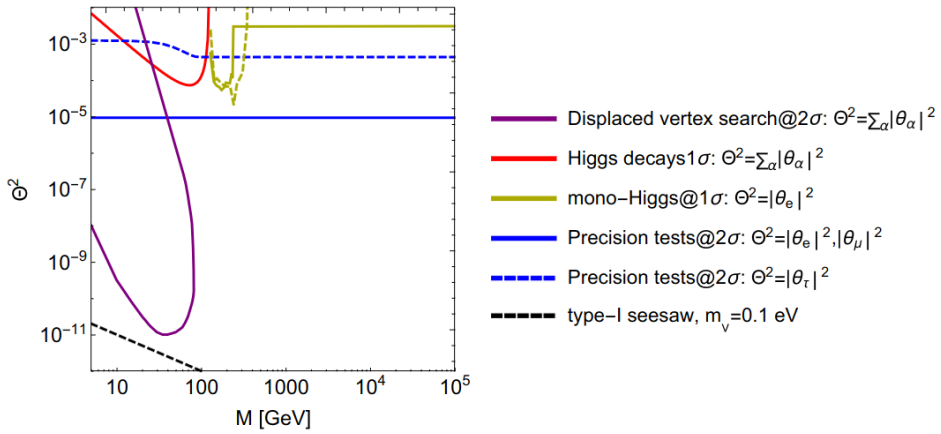

Figure 1.7: Sensitivities of various observables to the mixing angle θ between active and sterile neutrinos and the mass of sterile neutrinos, M, at the FCC-ee. In addition to the primary signatures discussed earlier, this analysis also includes the sensitivities derived from Higgs boson decays and mono-Higgs production.

Moreover, various indications of physics beyond the SM point to the existence of novel sectors that may harbor new light particles. A prominent class of models, known as "neutral naturalness," attempts to elucidate why the weak scale remains insensitive to high-energy physics scales in nature. In these models, the particles that shield the Higgs boson mass from substantial quantum corrections are electrically neutral. Furthermore, these models often require some of these new particles to have low masses, making them potentially detectable through rare Higgs boson decays.

Additionally, the prospect of new neutral "hidden" sectors gains traction in many electroweak baryogenesis models, where modifications to the electroweak phase transition are achieved by introducing new neutral fields interacting with the Higgs boson.

Benefiting from the pristine detection environment and abundant samples of Z and Higgs bosons available at the FCC-ee, non-standard decays facilitated by the production of new hidden sector particles can be explored down to exceedingly small branching ratios. Figure 1.8 illustrates the outcomes of two dedicated investigations into exotic Z and Higgs boson decays [25, 26], where these decays occur via the production of novel hidden sector particles. For both bosons, the FCC-ee's potential to probe such hidden sectors significantly surpasses what can be achieved at the HL-LHC, with constraints in both cases akin to the rare decay constraints typically derived in lower-energy hadron physics experiments at the intensity frontier.

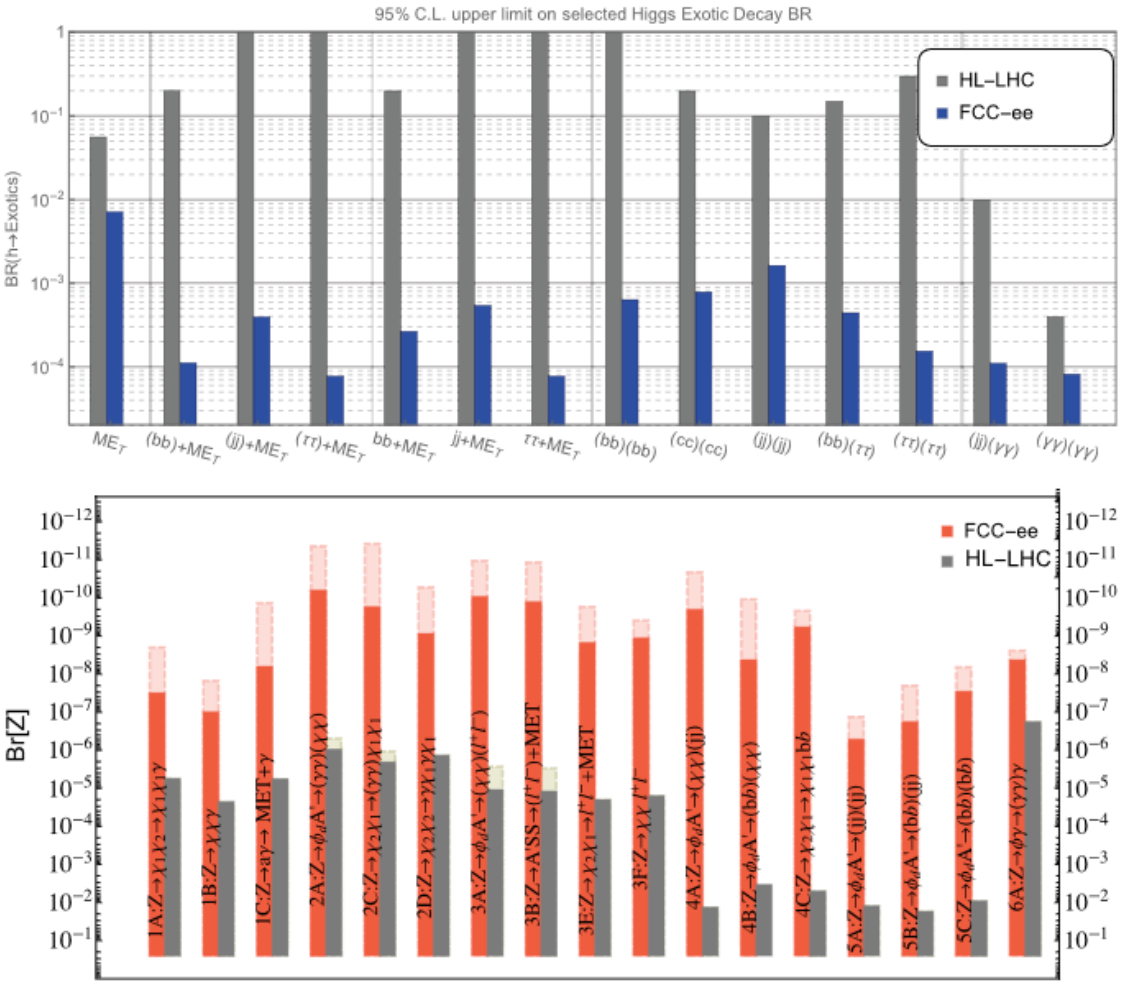

Figure 1.8: Expected upper limits on the branching ratios for the non-standard decays of the Higgs boson (top) and Z boson (bottom), accessible at the FCC-ee collider, including decays involving particles from the dark matter sector [25, 26]. [The availability of large, experimentally clean samples of these bosons enables the detection of rare non-standard decays, even for extremely small branching ratios.] The figures also display the expected limits for exotic Z boson decays under both worst-case (light-red) and best-case (red) scenarios.

Lepton flavour violating Z decays

The observation of flavor-violating Z decays, such as $Z \to e\mu$, $\mu\tau$, or $e\tau$, would constitute compelling evidence for physics beyond the Standard Model (SM). These decays are strictly forbidden in the SM due to the GIM mechanism [27] and their predicted branching fractions remain extremely minuscule (below 10^{-50}) even when the SM is extended to accommodate flavor violation in the neutral lepton sector (LFV), induced by the leptonic mass mixing matrix [28]. The emergence of significant rates for these LFV processes, $Z \to \ell_1\ell_2$, could therefore signify the presence of new particles like right-handed neutrinos. The quest for LFV Z decays also complements direct searches for heavy neutral leptons.

A phenomenological investigation [29] explores the FCC-ee's potential to probe the existence of sterile neutral fermions in light of improved determinations of neutrino oscillation parameters, fresh constraints on low-energy LFV observables, and cosmological limits. This study also addresses the synergy between these searches and the current and anticipated precision of similar experiments at lower energies. The most potent sensitivity for detecting or constraining LFV in the $e\mu$ sector arises from experiments focused on muon-electron conversion in nuclei. In contrast, the examination of decays $Z \to e\tau$ and $Z \to \mu\tau$ offers invaluable and unique insights into connections with the third generation.

The prevailing limits on branching ratios for charged lepton flavor-violating Z decays were set by the LEP experiments. More recently, the ATLAS experiment has improved the bounds for $e\mu$ final states. Typical upper limits on branching fractions lie within the range of 10^{-5} to 10^{-6}. The FCC-ee's production of 5×10^{12} Z decays substantially enhances these limits by several orders of magnitude and scrutinizes scenarios of beyond-the-SM physics, probing branching fractions down to 10^{-9} [30].

Chapter 2

IDEA detector concept

The IDEA detector concept, specifically developed for the FCC-ee experiment, utilizes well-established technologies that have been refined through years of research and development (R&D). Nonetheless, further efforts are required to finalize and optimize the detector design. Figure 2.1 provides an overview of the IDEA detector's structure, while Table 2.1 presents its essential parameters. The detector includes a silicon pixel vertex detector, a sizeable yet exceptionally lightweight short-drift wire chamber surrounded by a layer of silicon micro-strip detectors, a superconducting solenoid coil with minimal mass, a pre-shower detector, a dual-readout calorimeter, and muon chambers positioned within the magnet return yoke.

Table 2.1: Key parameters of the IDEA detector.

Parameter	**Value**
Vertex technology	Silicon
Vertex inner/outer radius	1.7 cm / 34 cm
Tracker technology	Drift chamber + silicon wrapper
Tracker half length/outer radius	2.0 m / 2.0 m
Solenoid bore radius/half length	2.1 m / 3.0 m
Preshower/calorimeter absorber	Lead/lead
Preshower inner/outer radius	2.4 m / 2.5 m
DR calorimeter inner/outer radius	2.5 m / 4.5 m
Overall height/length	11 m / 13 m

2.1 IDEA vertex detector

The innermost detector, surrounding the beam pipe, is a silicon pixel detector. Recent test-beam results on the detectors planned for the ALICE ITS upgrade, based on the

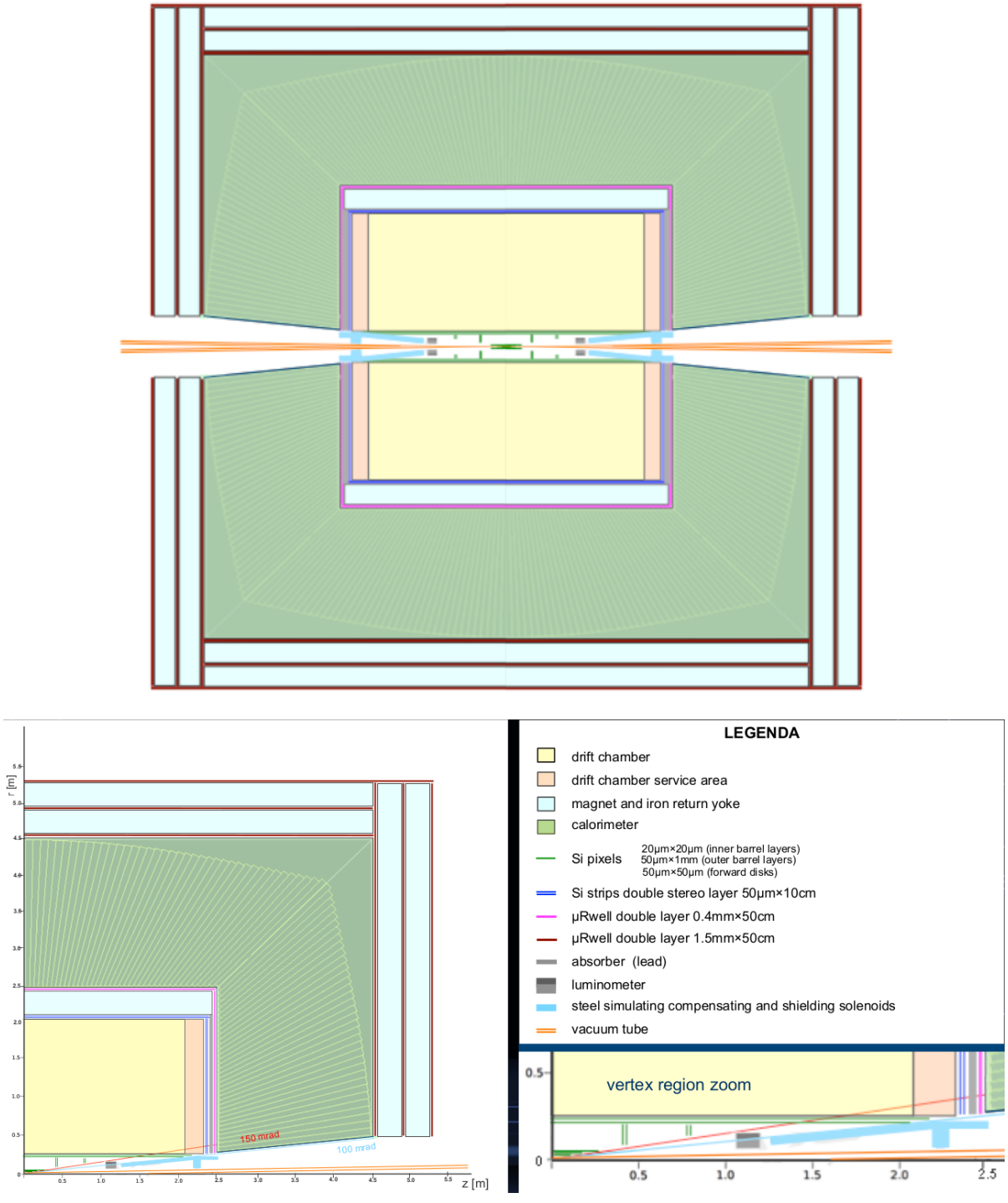

Figure 2.1: Layout of the IDEA detector for FCC-ee.

ALPIDE readout chip[31], indicate an excellent (∼5 μm) resolution, high efficiency at low power, and low dark-noise rate. These very light detectors, 0.3 (1.0)% X_0 per innermost (outermost) layer, are the basis for the IDEA vertex detector. Table 2.2 defines the vertex detector parameters.

Table 2.2: Vertex detector parameters.

Barrel							
Layer	R [mm]	L [mm]	Si eq. thick. [μm]	X_0 [%]	pixel size [mm^2]	area [cm^2]	# of channels
1	17	±110	300	0.3	0.02×0.02	235	60M
2	23	±150	300	0.3	0.02×0.02	434	110M
3	31	±200	300	0.3	0.02×0.02	780	200M
4	200	±2040	450	0.5	0.05×1.0	52K	105M
5	220	±2240	450	0.5	0.05×1.0	62K	124M

Endcap								
Disk	R_{in} [mm]	R_{out} [mm]	z [mm]	Si eq. thick. [μm]	X_0 [%]	pixel size [mm^2]	area [cm^2]	# of channels
1	42	190	±400	300	0.3	0.05×0.05	2.2K	87M
2	44	190	±420	300	0.3	0.05×0.05	2.2K	86M
3	78	190	±760	300	0.3	0.05×0.05	1.9K	76M
4	80	190	±780	300	0.3	0.05×0.05	1.9K	75M

2.2 IDEA drift chamber

The drift chamber (DCH) is designed to provide good tracking, high-precision momentum measurement, and excellent particle identification by cluster counting. The main peculiarity of this chamber is its high transparency in terms of radiation lengths, obtained as a result of the novel approach adopted for the wiring and assembly procedures[32]. The total amount of material in the radial direction towards the barrel calorimeter is of the order of 1.6% X_0, whereas, in the forward direction, it is about 5.0% X_0, 75% of which are in the end plates instrumented with the front-end electronics.

The DCH is a unique-volume, high-granularity, all-stereo, low-mass, cylindrical, short-drift, wire chamber, co-axial with the 2 T solenoid field. It extends from an inner radius $R_{\text{in}} = 0.35$ m to an outer radius $R_{\text{out}} = 2$ m, for a length $L = 4$ m and consists of 112 co-axial layers, at alternating-sign stereo angles, arranged in 24 identical azimuthal sectors. The approximately-square cell size varies between 12.0 and 14.5 mm for a total of 56,448 drift cells. The challenges potentially arising from a large number of wires are addressed by the peculiar design of the wiring, which was successfully employed for the recent construction of the MEG2 [33] drift chamber.

The chamber is operated with a very light gas mixture, 90% He – 10% iC_4H_{10} (isobutane), corresponding to a maximum drift of ∼400 ns. The number of ionization clusters generated by a minimum ionizing particle (m.i.p.) is about 12.5 cm^{-1}, allowing

cluster counting/timing techniques to be employed to improve both spatial resolution ($\sigma_x < 100\mu$m) and particle identification ($\sigma(dN_{\rm cl}/dx)/(dN_{\rm cl}/dx) \approx 2\%$).

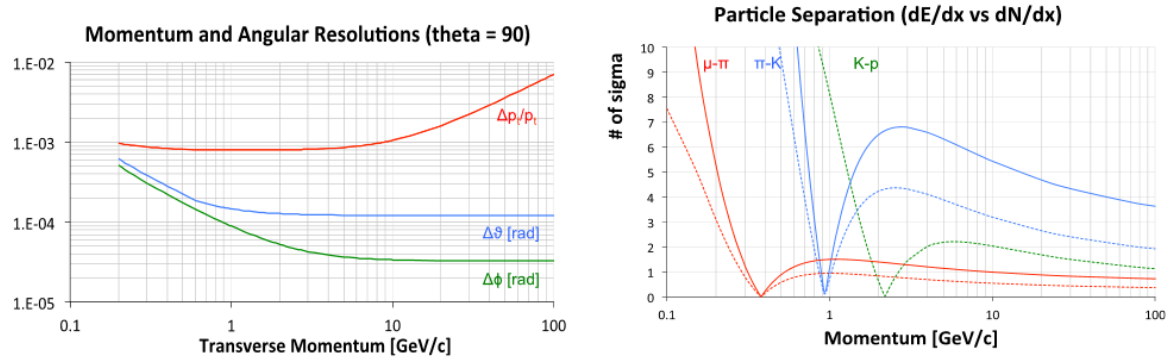

Figure 2.2: IDEA drift chamber performance. Left: momentum and angular resolutions for $\theta = 90°$ as a function of momentum. Right: particle type separation in units of standard deviations as a function of momentum, with cluster counting (solid curves) and with dE/dx (dashed curves).

The angular coverage extends down to $\sim 13°$, and could be further extended with additional silicon disks between the DCH and the calorimeter end caps. A drift distance resolution of 100 μm has been obtained in a MEG2 drift chamber prototype [34](7 mm cell size), with a very similar electrostatic configuration and gas mixture. A better resolution is expected for the DCH, as a result of the longer drift distances and the employment of cluster timing techniques. Analytical calculations for the expected momentum, transverse momentum, and angular resolutions, conservatively assuming a 100 μm point resolution, are plotted in the left panel of Figure 2.2.

The expected particle identification performance is presented in the right panel of Figure 2.2. Results are based on cluster counting, where it is assumed that the relative resolution on the measurement of the number of primary ionization clusters ($N_{\rm cl}$) equals $1/\sqrt{N_{\rm cl}}$. For the whole range of momenta, particle separation with cluster counting outperforms the dE/dx technique by more than a factor of two. The expected pion/kaon separation is better than three standard deviations for all momenta except in a narrow range from 850 MeV to slightly above 1 GeV.

A layer of silicon micro-strip detectors surrounds the outside of the drift chamber, providing an additional accurate space point as well as precisely defining the tracker acceptance.

The detailed parameters of the drift chamber are listed on Tables 2.3 and 2.4.

Table 2.3: Drift chamber parameters.

Dimensions			
	R_{in} [mm]	R_{out} [mm]	z [mm]
Drift Chamber	235	2080	$\pm$2080
Service Area	235	2080	$\pm$2080:2330

Thicknesses and X_0 Values					
	Inner Wall [mm]	Gas [mm]	Wires [mm]	Outer Wall [mm]	Service Area [mm]
Thickness [mm]	0.2	1000	1000	20	250
X_0 [%]	0.08	0.07	0.13	1.2	4.5

# of Layers	176	min 8.25 mm – max 10.37 mm
# of Cells	122512	192 at 1st – 1200 at last layer
Average Cell Size	9.82 mm	min 8.25 mm – max 10.37 mm
Average Stereo Angle	141 mrad	min 32 mrad – max 249 mrad
Transverse Resolution	100 µm	80 µm with cluster timing
Longitudinal Resolution	750 µm	600 µm with cluster timing
Active Volume	56 m^3	
Readout Channels	245,024	readout from both ends
Max Drift Time	350 ns	700 $\times$ 8 bit at 2 GHz

Table 2.4: Drift chamber extra parameters.

Table 2.5: Silicon Wrapper Parameters.

Barrel							
Layer	R [mm]	L [mm]	Si eq. thick. [μm]	X_0[%]	Pixel size [mm^2]	Area [cm^2]	# of channels
1	2100	±2400	450	0.5	0.05×100	616K	12.3M
2	2120	±2400	450	0.5	0.05×100	620K	12.4M

Endcap								
Disk	R^{in} [mm]	R^{out} [mm]	z [mm]	Si eq. thick. [μm]	X_0[%]	Pixel size [mm^2]	Area [cm^2]	# of channels
1	240	2080	±2400	450	0.5	0.05×100	268K	5.4M
2	242	2080	±2400	450	0.5	0.05×100	268K	5.4M

2.3 IDEA Silicon-wrapper

The primary role of the silicon wrapper subdetector is to provide precise and efficient tracking of charged particles, aiding in the reconstruction of their trajectories and momentum measurements.

The IDEA silicon wrapper offers a precise 3D position measurement at the particles' exit point from the central drift chamber. It opens the possibility to provide an absolute reference for the calibration of the polar angle measurement and hence define precisely the angular acceptance. The wrapper encapsulates the tracker in both the barrel and forward regions. In addition, if the silicon provides timing information, this can complement the PID (Particle Identification) range missing from IDEA by providing a time-of-flight detector. For instance, to cover the pion/kaon loss of discrimination around 1 GeV, a timing of 0.5 ns at 2 m just outside the drift chamber would be sufficient to recover the performance. An improved time resolution could strengthen the PID up to 5 GeV. Such a timing measurement will also be valuable for the reconstruction of secondary vertices in the search or discovery of massive long-lived particles. Table 2.5 shows the parameters of Si-Wrapper sub-detector.

2.4 IDEA preshower

A preshower detector is located between the magnet and the calorimeter in the barrel region and between the drift chamber and the end-cap calorimeter in the forward region. Table 2.6 shows the preshower parameters. In the barrel region, the magnet coil works as an absorber of about $1X_0$ and is followed by one layer of μRWELL chambers; a second layer of chambers follows after another $1X_0$ of lead. A similar construction occurs in the forward region, however, here with both absorber layers made are from lead.

The μRWELL chamber layers provide an accurate determination of the impact point of both charged particles, and therefore define the tracker acceptance volume with precision. A further details on μRWELL will be discussed in chapter 3. There is also further improvement in the tracking resolution. In addition, a large fraction of the π^0s

can be tagged by having both photons from their decay identified by the preshower. The optimization of the preshower system and the evaluation of its performance is in progress.

Table 2.6: Preshower parameters.

Barrel						
Layer	R [mm]	L [mm]	Thickness [mm]	Pixel size [mm^2]	Area [cm^2]	# of channels
μRwell	2440	$\pm$2500	20	0.4×500	785K	392K

Endcap							
Disk	R^{in} [mm]	R^{out} [mm]	z [mm]	Thickness [mm]	Pixel size [mm^2]	Area [cm^2]	# of channels
μRwell	248	2420	$\pm$2500	20	0.4×500	370K	185K

2.5 IDEA dual-readout calorimeter

A lead-fibre dual-readout calorimeter [35] surrounds the second preshower layer with parameters listed in Table 2.7. This calorimeter concept has been extensively studied and demonstrated over ten years of R&D by the DREAM/RD52 collaboration [36, 37]. Figure2.3 shows the different calorimeter structures. The calorimeter is 2 m deep, which corresponds to approximately $7\lambda_I$. Two possible layouts have been implemented in the simulation for a realistic 4π detector. Both cover the full volume down to 100 mrad of the z axis, with no inactive region. In the first configuration, the calorimeter is made of truncated rectangular-base pyramidal towers with 92 different sizes. In the second, it is built with rectangular prisms coupled to pyramidal towers. The total number of fibers is of the order of 10^8 in both cases.

The dual-readout calorimeter is sensitive to the independent signals from scintillation light (S) and Čerenkov light (C) production, resulting in an excellent energy resolution for both electromagnetic and hadron showers. By combining the two signals, the resolution estimated from GEANT4 simulations is found to be close to $10\%/\sqrt{E}$ for isolated electrons and $30\%/\sqrt{E}$ for isolated pions with negligible constant terms.

The dual-readout calorimeter provides very good intrinsic discrimination between muons, electrons/photons, and hadrons for isolated particles. Figure 2.4 demonstrates a nearly perfect separation in the C/S ratio for 80 GeV electrons and protons: for an electron efficiency of 98%, a simulated rejection factor of up to 600 can be reached for isolated protons. The rejection factor in jets remains to be evaluated experimentally. In addition to the C/S ratio, a few other variables, like the lateral shower profile, the starting time of the signal, and the charge-to-amplitude ratio, can be used to enhance the intrinsic calorimeter particle separation performance[38].

In addition to the intrinsic particle identification capabilities, the fine transverse granularity allows close showers to be separated and provides good matching to tracks

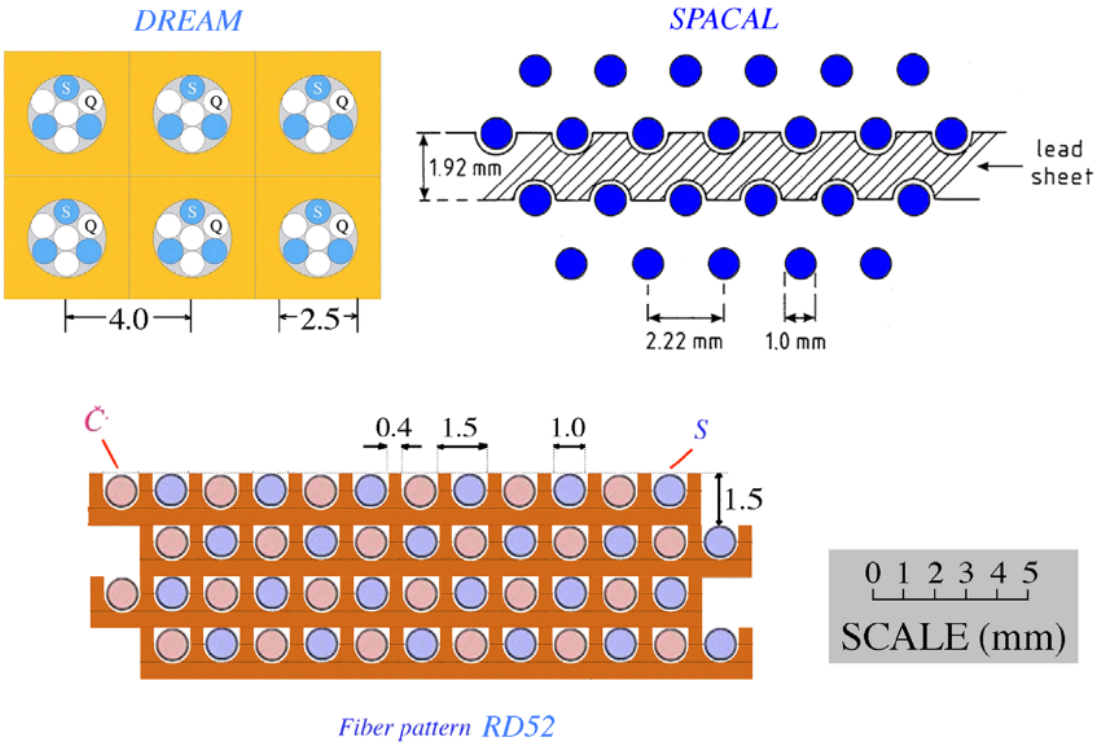

Figure 2.3: The structure of the new RD52 calorimeter (copper-based modules), compared to that of two other fiber calorimeters: DREAM and SPACAL. Image from reference[38].

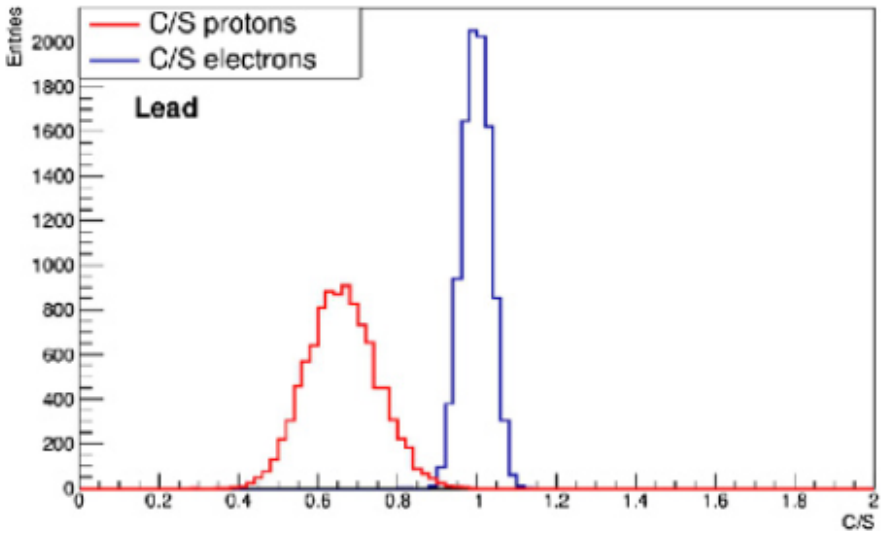

Figure 2.4: Particle identification performance of the dual-readout calorimeter: C/S ratio for 80 GeV isolated electrons and protons.

in the inner, preshower signals, and also to muon tracks, making this calorimeter a good candidate for efficient particle-flow reconstruction. The need for disentangling signals produced by overlapping electromagnetic and hadron showers is likely to require longitudinal segmentation as well. Several ways to implement this segmentation are envisioned and are being studied, e.g., the classical division of the calorimeter into several compartments, an arrangement with fibers starting at different depths, the extended use of the timing information, etc. The specific advantages and drawbacks of each approach need to be studied through both simulations and beam tests.

Table 2.7: Dual-readout calorimeter parameters.

Barrel			
R [mm]	L [mm]	Thickness [mm]	Int. length
2500	±2500:4500	2000	8

Endcap				
R^{in} [mm]	R^{out} [mm]	z [mm]	Thickness [mm]	Int. length
±252:454	±2500:4500	±2500:4500	2000	8

Table 2.8: Muon system parameters.

Barrel							
Layer	R [mm]	L [mm]	Thickness [mm]	Int. length	Pixel size [mm^2]	Area [cm^2]	# of channels
μRwell	4520	±4500	20		1.5×500	2.6M	341K
Iron	4560	±4500	300	1.5			
μRwell	4880	±4500	20		1.5×500	3.0M	386K
Iron	4920	±4500	300	1.5			
μRwell	5240	±5260	20		1.5×500	4.3M	462K

Endcap								
Disk	R^{in} [mm]	R^{out} [mm]	z [mm]	Thickness [mm]	Int. length	Pixel size [mm^2]	Area [cm^2]	# of channels
μRwell	700	5200	±4520	20		1.5×500	1.9M	227K
Iron	700	5200	±4560	300	1.5			
μRwell	700	5200	±4880	20		1.5×500	1.9M	227K
Iron	700	5200	±4920	300	1.5			
μRwell	700	5200	±5240	20		1.5×500	1.9M	227K

2.6 IDEA muon system

The IDEA detector concept foresees a muon detection system[39] that would be realized using the μRWELL technology (which will be described in details in the following chapter). The muon detector would follow the IDEA geometry with a central cylindrical barrel region closed at the two extremities by two endcaps to ensure hermeticity. In the barrel, there will be three muon stations, at increasing radial distance from the interaction point, housed within the iron yoke that closes the solenoidal magnetic field. Each station will consist of a large mosaic of μRWELL detectors. In order to profit from the industrial production capabilities of this technology, a modular design has been adopted. The basic μRWELL "tile" will have an active area of $50 \times 50\,\mathrm{cm}^2$. The two layers of strips will both have a strip pitch of 1 mm, giving a total of 500×2 strips and consequently 1000 readout channels per tile. The muon system dimensions and parameters are listed in Table 2.8.

Chapter 3

μRWELL detector technology

The μ-RWELL [40]detector technology is a micropattern gaseous detectors (MPGD) born in 2014. It is often introduced with the following tagline: "a compact, robust, spark protected, resistive MPGD," a sentence that embodies the core concepts of this technology. The modern photolithographic technology on flexible and standard PCB supports has allowed the invention of novel and robust MPGDs, such as gas electron multiplier (GEM) [41], The thick gas electron multiplier (THGEM) [42] and Micromegas [43]. These detectors exhibit good spatial and time resolution, high rate capability, large sensitive area, flexible geometry, good operational stability, and radiation hardness. However, due to the fine structure and the typical micrometric distance of their electrodes, MPGDs generally suffer from spark occurrence that can eventually damage the detector. The generation of the sparks in gas detectors is correlated with the transition from avalanche to streamer. This transition occurs when the Raether limit is overcome, that is when the primary avalanche size exceeds 10^7–10^8 ion-electron pairs. In MPGDs, due to the very small distance between the anode and cathode electrodes, the formation of the streamer can be easily followed by a discharge. For GEMs, the adopted solution is to share the gain among multiple amplification stages (double or triple-GEM structures), which allows a considerable reduction of the discharge rate. For Micromegas, the problem of the spark occurrence between the metallic mesh and the read-out PCB has been solved with the introduction of a resistive layer deposition realized on top of the readout itself. The principle is the same as the resistive electrode used in Resistive Plate Counters (RPCs) [44]: the streamer, discharging a limited area around its location, is automatically quenched and the transition to spark is strongly suppressed, giving the possibility to achieve large gains.

A further limitation of such MPGDs is correlated with the complexity of their assembly procedure. In particular, a GEM chamber requires some time-consuming assembly steps such as the stretching and the gluing of the GEM foils. For this detector there is a recently proposed solution based on the so-called NS2 assembly approach [45]: an evolution of the stretching technique introduced for the GEM chambers of the LHCb

experiment. Similar considerations can be also made for Micromegas, where the metallic mesh, defining the detector amplification region, requires precise stretching.

The main goal of this project is the development of a novel MPGD by combining in a unique approach the solutions and improvements realized in the last years in the MPGD field: a very compact detector structure, robust against discharges and exhibiting large gains (up to 10^4), easy to build, cost-effective and suitable for mass production. The novel detector, which is called micro-resistive WELL (μ-RWELL), has some features (such as electric field shape and signal formation) in common with some MPGDs developed by the end of the last century. The prototype discussed in this work, designed at the Laboratori Nazionali di Frascati and realized in the 2009 by TE-MPE-EM Workshop at CERN (with a declared resistivity of 100 MOhm/$\square$), has been developed in parallel with the CERN-GDD group.

3.1 Detector description

The μ-RWELL is a single-amplification stage resistive MPGD composed of two elements, as shown in Figure 3.1: the cathode, a simple PCB with a thin copper layer on one side, and the μ-RWELL_PCB, the core of the detector. The baseline version of the μ-RWELL_PCB is a multi-layer circuit realized by means of standard photo-lithography technology. It is composed of three layers: a well-patterned single copper-clad polyimide (Apical®) foil acting as the amplification element of the detector; a resistive layer realized with a Diamond-Like-Carbon (DLC) film sputtered on the bottom side of the polyimide foil working as the discharge limitation stage; a standard PCB for readout purposes, segmented as strip, pixel, or pad electrodes.

Applying a suitable voltage between the copper layer and the DLC, the well acts as a multiplication channel for the ionization produced in the drift gas gap, as illustrated in Figure 3.2. Besides the suppression of the streamer-to-discharge transition, with a mechanism similar to that of the Resistive Plate Counters (RPC [44]), the presence of the DLC affects the rate capability and the space resolution of the detector. In particular, concerning the effects on the space resolution, the charge induced on the resistive film is spread with a time constant that depends on the surface resistivity (hereafter simply called resistivity) and the capacitance per unit area between the resistive layer and the readout plane. As shown in [46], the best space resolution (~50 μm) with a strip-pitch of 400 μm and particles crossing the detector perpendicular to the readout plane has been achieved with a DLC resistivity of approximately 100 M$\Omega/\square$, using the classical charge centroid (CC) method for position reconstruction.

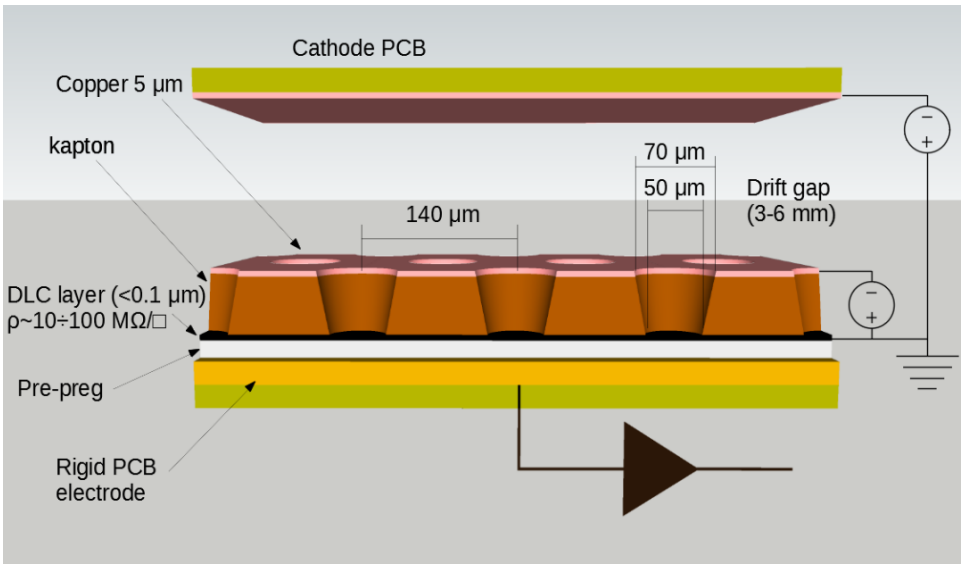

Figure 3.1: Baseline layout of the μ-RWELL, this figure is taken from [47].

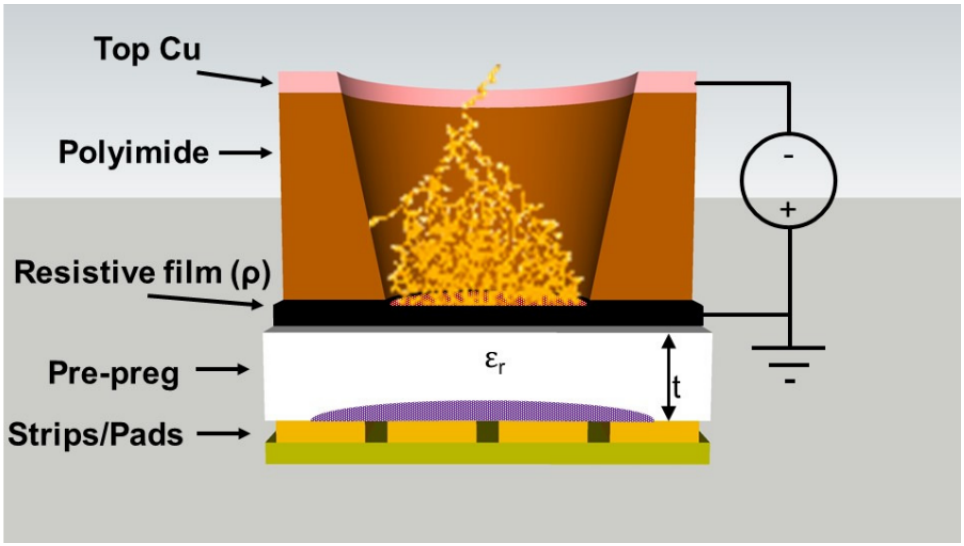

Figure 3.2: Principle of operation of the μ-RWELL detector, this figure is taken from [47].

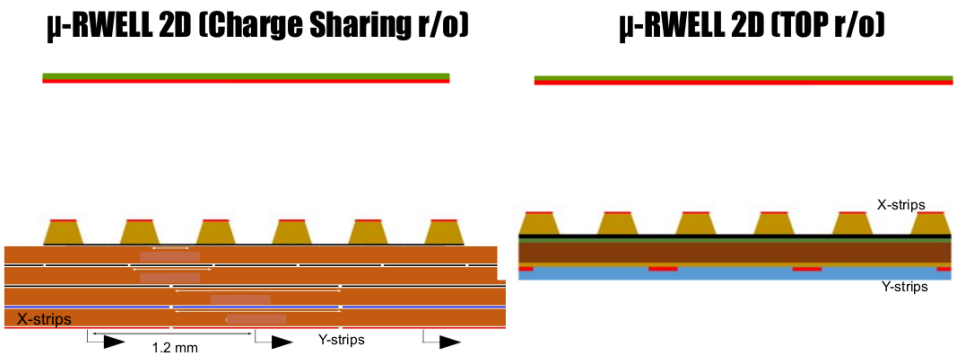

Figure 3.3: Charge sharing and TOP layouts.

3.2 Detector Research and Development (R&D)

In this section, we discuss the research and development (R&D) activities related to μRWELL (Micro-Resistive WELL) detector technology. The μRWELL detector technology is proposed for both the pre-shower and the muon system of the IDEA detector concept.

3.2.1 Involvement in test beam activities

As part of the R&D efforts, I had the opportunity to actively contribute to the development of μRWELL detector technology by participating in two test beam activities at CERN, specifically at beamlines H8 and H4. These test beams were instrumental in characterizing the performance of the detectors and advancing the technology.

Test beam at CERN H8

In June 2023, we collaborated with external groups, including researchers from Ferrara and LNF, to conduct a test beam at CERN's H8 beamline. During this test beam, the first two prototypes of double-sided readout μRWELL detectors were subjected to rigorous testing. These two prototypes have different configurations called: **TOP readout**, and **Charge sharing readout** these two distinct 2D layout configurations for μRWELL detectors are optimized for specific purposes. Figure 3.3 shows the differences between both configurations. These detectors underwent extensive testing using high-energy muon and pion beams at CERN's H8 SPS (Super Proton Synchrotron). Various high-voltage settings were explored with the goal of studying the spatial resolution and efficiency of the detectors.

The preliminary results obtained with the 2D-layout configurations were highly promising and encouraging. Notably, Figure 3.5 shows the very preliminary results of this test

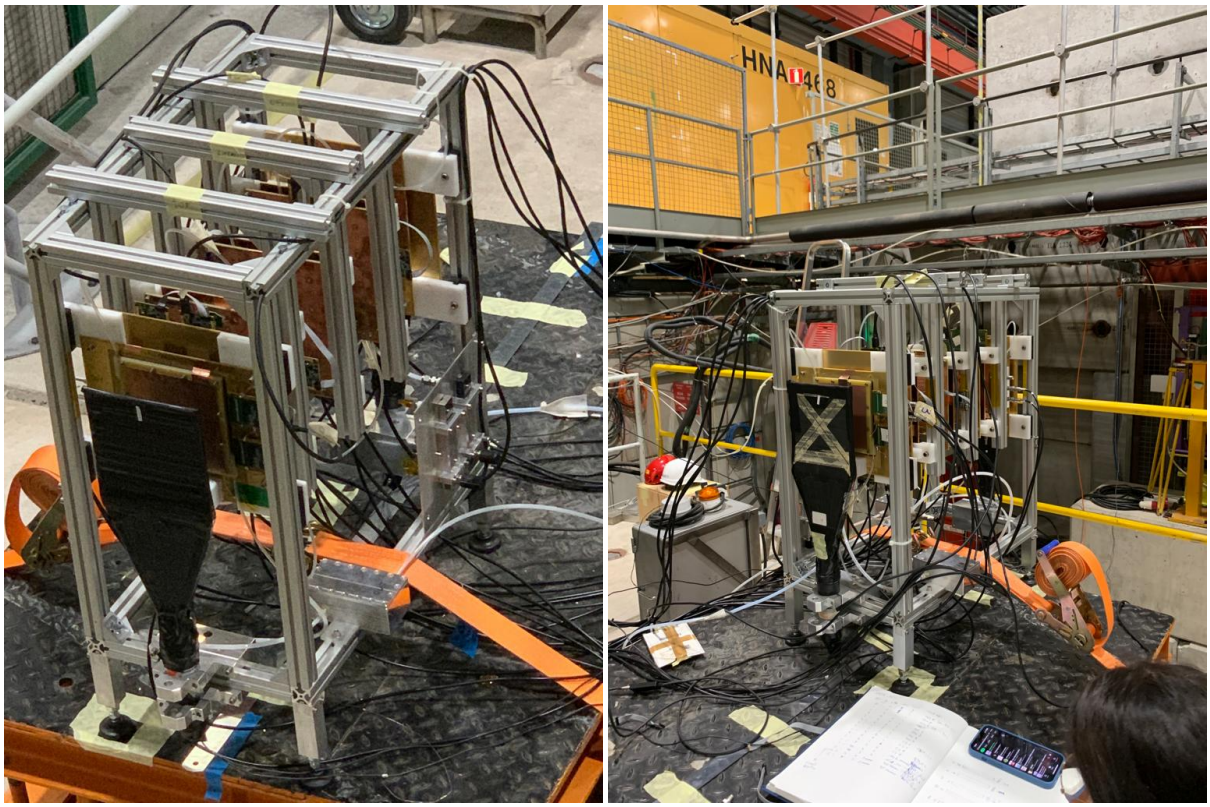

Figure 3.4: CERN H8 test beam setup.

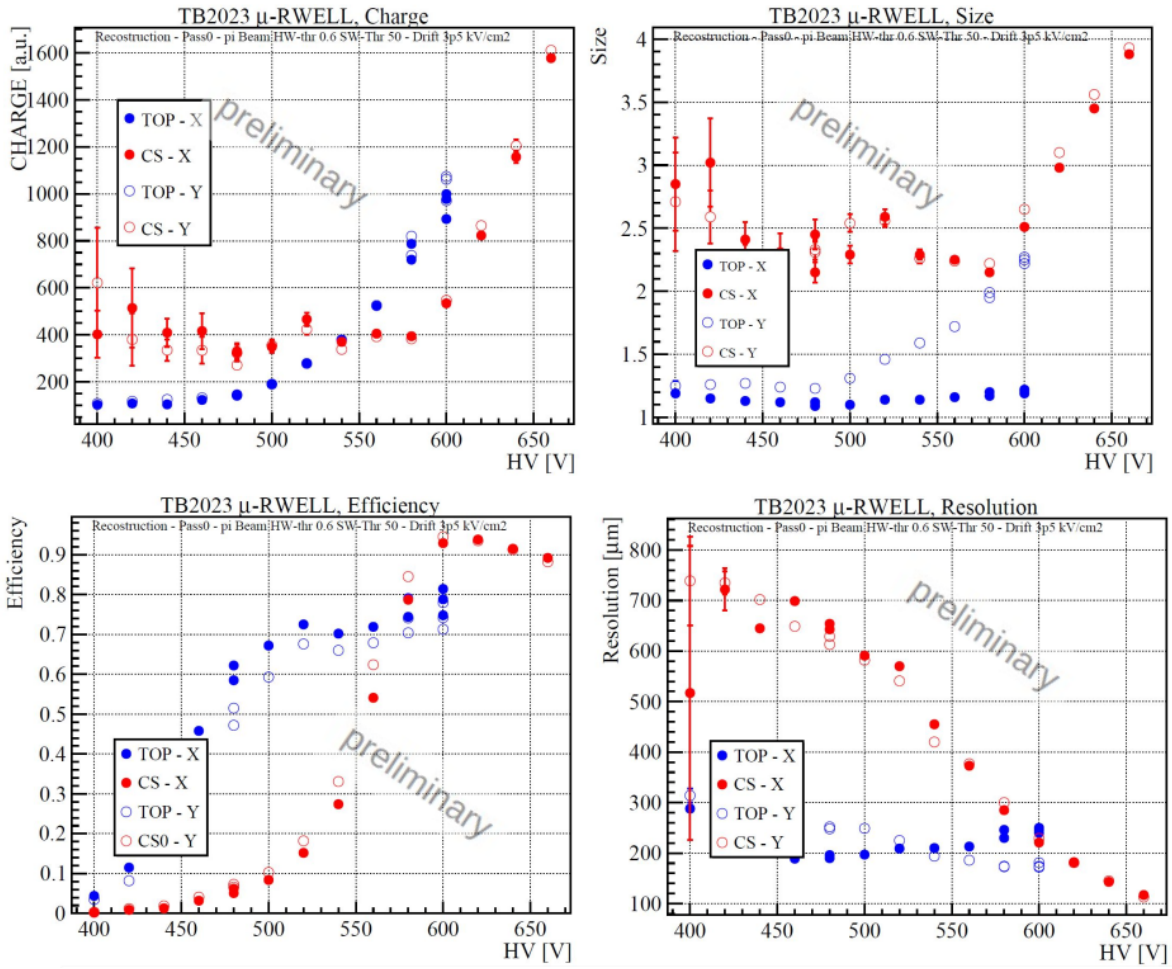

Figure 3.5: Scanning the two layouts over high voltage.

beam, and I shall describe them in the following lines:

Both layouts are represented with 10 * 10 cm^2 active area detectors. In the same setup we used other four detectors for tracking, event selection and alignments, and two scintillators for triggering. And the preliminary results for these two layouts are the following:

- **TOP r/o** does not share the signal charge between X and Y. On the X (TOP), its cluster size is fixed, and the spatial resolution is digital; while on the Y, it has a standard behavior, and thanks to the charge diffusion (DLC), the spatial resolution improves with the gain. TOP r/o reaches the efficiency plateau at lower HV values, but it is affected by the segmentation of the TOP.

- **CS r/o** shares the signal charge between X and Y. The charge-sharing mechanics

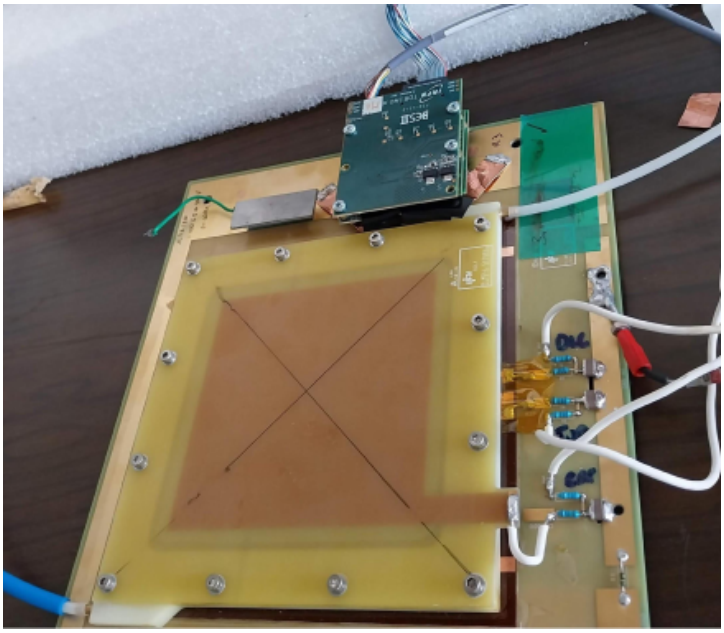

Figure 3.6: TIGER/GEMROC readout system installed to a 10x10 cm^2 μRWELL prototype.

work properly, and it increases the cluster size up to 4; this improves the spatial resolution up to 100 μm. CS r/o reaches an efficiency greater than 95%.

Test beam at CERN H4

In August 2023, we embarked on another important test beam activity, this time at CERN's H4 beamline. During this test beam, we focused on conducting experiments with μRWELL detectors using TIGER/GEMROC [48] readout systems as shown in Figure 3.6.

The results obtained from the H4 test beam provided valuable insights into the performance and capabilities of μRWELL detectors when coupled with specific readout systems. These findings instilled confidence that there are further opportunities for enhancing the design and performance of the detectors.

3.2.2 Moving towards larger detectors

Based on the promising results obtained from the aforementioned test beam activities, our R&D efforts are now poised to transition to the development of larger μRWELL detectors, specifically with dimensions of 50x50 cm^2. This expansion represents a significant step forward in the evolution of μRWELL technology, and it opens up new avenues for research and applications.

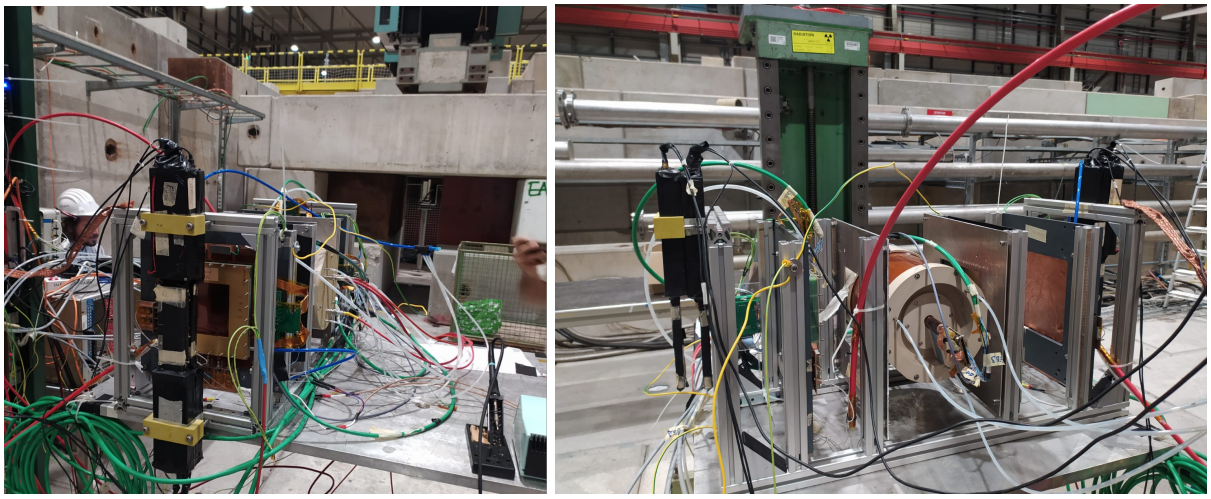

Figure 3.7: CERN H4 test beam setup.

On the other hand, in our laboratory at INFN-Bologna, we have the largest μRWELL chamber ever built, shown in Fig 3.8. I have actively participated in testing this remarkable chamber using cosmic rays. This hands-on experience allowed me to gain valuable insights into the performance and characteristics of μRWELL detectors, contributing to our understanding of their capabilities and potential applications.

The experience gained from the test beams and the continuous commitment to innovation ensure that the R&D efforts in μRWELL detector technology will contribute significantly to the advancement of detector systems for future experiments, including those at the cutting-edge IDEA detector.

Figure 3.8: The largest μRWELL chamber.

Chapter 4

GEANT4 full simulation for IDEA detector concept

4.1 Introduction to Geant4

Geant4 [49] is a Monte Carlo simulation toolkit for the simulation of the passage of particles through matter. It is a general-purpose toolkit that can be used to simulate a wide range of physics processes, including the interactions of particles with matter, the transport of particles, and the detection of particles. Geant4 is a powerful and flexible toolkit that is used in a wide variety of fields, including high energy physics, nuclear physics, medical physics, and space physics.

Geant4 is based on the Monte Carlo method. The Monte Carlo method is a statistical method that is used to solve problems by sampling from a probability distribution. In Geant4, the Monte Carlo method is used to simulate the physical processes that occur when a particle interacts with matter.

Geant4 provides a variety of features that make it a powerful and flexible toolkit for particle transport and simulation. These features include:

- A wide range of physics models for the simulation of particle interactions with matter.
- A flexible geometry model that can be used to describe a wide variety of detector geometries.
- A powerful event generator that can be used to generate events for a variety of physics processes.
- A variety of output tools that can be used to analyze the results of simulations.

4.1.1 Using Geant4 in High Energy Physics

Geant4 is a powerful toolkit for the simulation of the passage of particles through matter. It is widely used in high energy physics to simulate the interactions of particles with detectors. Geant4 provides a variety of features that make it a powerful tool for high energy physics simulations, including a wide range of physics models for the simulation of particle interactions with matter, including the interactions of photons, electrons, hadrons, and ions, a flexible geometry model that can be used to describe a wide variety of detector geometries, including complex detectors such as the CMS and ATLAS detectors at the LHC, a powerful event generator that can be used to generate events for a variety of physics processes, such as electron-positron annihilation and proton-proton collisions, and variety of output tools that can be used to analyze the results of simulations, such as histograms and event displays.

Geant4 is used in high energy physics to simulate a wide range of physics processes; The production and decay of particles, the interactions of particles with detectors, and the response of detectors to particles.

Geant4 is also used in high energy physics to design and optimize detectors. For example, Geant4 can be used to simulate the performance of a detector in a given environment or to optimize the design of a detector for a specific physics measurement.

Here is a brief overview of the steps involved in using Geant4 for a high energy physics simulation:

1. Define the detector geometry: This can be done using the Geant4 geometry model or by importing a CAD drawing of the detector.

2. Define the physics processes: Geant4 provides a variety of physics models for the simulation of particle interactions with matter. The user must select the physics models that are relevant to the simulation. Here are some examples of GEANT4 physics lists:

   FTFP-BERT: This physics list is a general-purpose option and stands for "Fritiof + Bertini Cascade." It combines the Fritiof model for high-energy hadronic interactions with the Bertini model for low-energy interactions, providing a broad range of capabilities for simulating particle interactions.

   QGSP-BERT: This physics list, which stands for "QGS + Bertini Cascade," is also a general-purpose option. It employs the Quark-Gluon String model (QGS) for high-energy interactions and the Bertini cascade model for low-energy interactions.

3. Generate events: Geant4 provides a powerful event generator that can be used to generate events for a variety of physics processes. The user must specify the parameters of the event generator, such as the type of particles to generate and their energies.

4. Simulate the events: Geant4 uses the physics models and the detector geometry to simulate the passage of particles through the detector.

5. Analyze the results: Geant4 provides a variety of output tools that can be used to analyze the results of simulations, such as histograms and event displays.

4.1.2 Main Classes Used in HEP Geant4

The main classes used in Geant4 applications are:

- **G4RunManager:** This class is responsible for managing the simulation run. It creates and initializes all of the necessary objects, such as the geometry, physics list, and event generator. It also controls the flow of the simulation.
- **G4GeometryManager:** This class manages the geometry of the simulation. It creates and stores the geometry objects, such as volumes, surfaces, and materials. It also provides methods for tracking particles through the geometry.
- **G4PhysicsList:** This class specifies the physics processes that are to be used in the simulation. It creates and initializes the physics models for these processes. It also provides methods for calculating the cross sections for these processes.
- **G4EventGenerator:** This class generates events for the simulation. It specifies the type and energy of the particles to be generated, as well as their initial positions and directions.
- **G4Track:** This class represents a particle track in the simulation. It stores the particle's type, energy, position, and direction. It also provides methods for tracking the particle through the geometry and for calculating its interactions with matter.

Other important classes used in HEP Geant4 include:

- **G4Material:** This class represents a material in the simulation. It stores the material's density, composition, and other properties.
- **G4Process:** This class represents a physics process in the simulation. It provides methods for calculating the cross section for the process and for simulating the interaction of a particle with matter.
- **G4Hit:** This class represents a hit on a detector in the simulation. It stores the position, time, and energy of the hit.
- **G4Step:** This class represents a step in the simulation. It stores the initial and final positions and energies of the particle, as well as the type of interaction that occurred.

4.2 Full simulation of IDEA detector concept

A full Geant4 simulation of the IDEA detector is being developed to study the performance of the detector and to optimize its design. The simulation is based on the detailed geometry of the IDEA detector. It is used to study the response of the IDEA detector to a variety of physics processes, including: Higgs boson production and decay, W boson and Z boson production and decay, top quark production and decay, and new particle searches.

The simulation results are used to optimize the design of the IDEA detector and to improve its performance. It will also be used to analyze data from the IDEA detector once it is operational. Here are some specific examples of how the full Geant4 simulation of the IDEA detector is being used:

- To study the track resolution of the IDEA tracker
- To study the energy resolution of the IDEA calorimeter
- To study the muon identification efficiency of the IDEA muon detector
- To study the background levels in the IDEA detector

In the following subsection, I shall talk about my thesis work and results in the Geant4 full simulation for IDEA detector concept.

4.2.1 Implementation of Si-Wrapper & Preshower subdetectors

Figure 4.1 shows an illustration (simple drawing, It is not a Geant4 visualization) for the preshower volume and dimensions, where the small white circle represents the beam-pipe, the yellow circle represents the vertex detector, green represents the drift chamber, and the red one represents the preshower volume. the black values represents the inner radii of the 3 detectors and the red ones represent the inner radii of the radiators.

First step, I have implemented the preshower volume dimensions. All 4 layers still in one big volume of preshower (**PSHW**).

The dimensions of the volume I have created are the following: $R_{in} = 2100.0mm, R_{out} = 2500.0mm$. Three layers with inner radii (2100 mm, 2120 mm, 2445 mm) with thicknesses (0.45 mm, 0.45 mm, 50 mm) respectively. One radiator layer with inner radius 2140 mm and thickness 300 mm, as shown in the following figure 4.1.

At this step, the dimensions of different sub-detectors are right. But all three sub-detectors (Si-Wrapper, Magnet, and Preshower) are still in one volume called Preshower. Two volumes needed to be implemented in the simulation:

- Si-Wrapper (SIWRP).
- Magnet (MGNT).

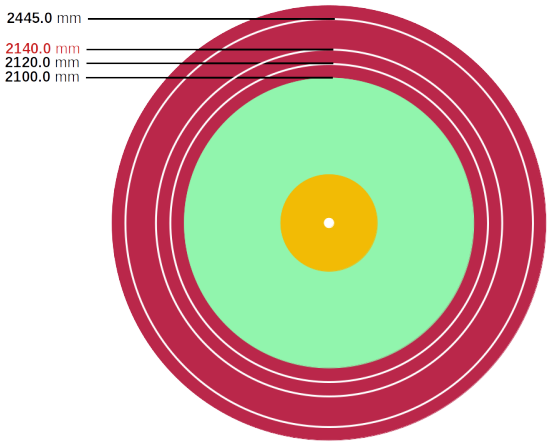

Figure 4.1: Dimensions of the Preshower volume.

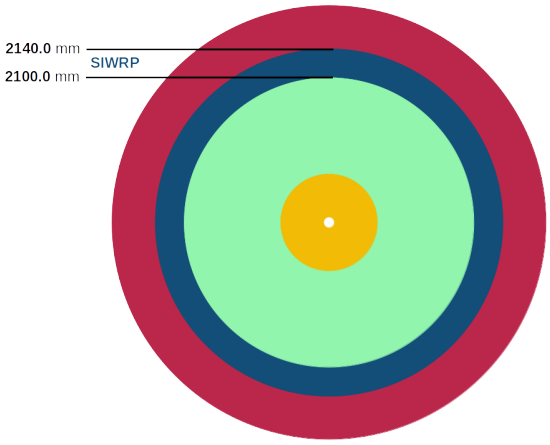

Figure 4.2: Illustration of the Si-Wrapper volume.

Si-Wrapper

Si-wrapper volume has been implemented with dimensions (R_{in}= 2100 mm, R_{out} = 2140 mm). Two layers have been defined at inner radii (2100 mm, 2120 mm), each layer with a thickness 0.45 mm. The new sub-detector volume have been assigned with the ladder. Figure 4.2 shows a drawing for the Si-Wrapper volume.

Magnet

Another volume (MGNT) has been added with dimensions (R_{in}= 2140 mm, R_{out}= 2440 mm). One passive layer volume with a thickness = 300 mm. Figure 4.3 shows a drawing for the Magnet volume, which hosts the magnetic field of the IDEA detector.

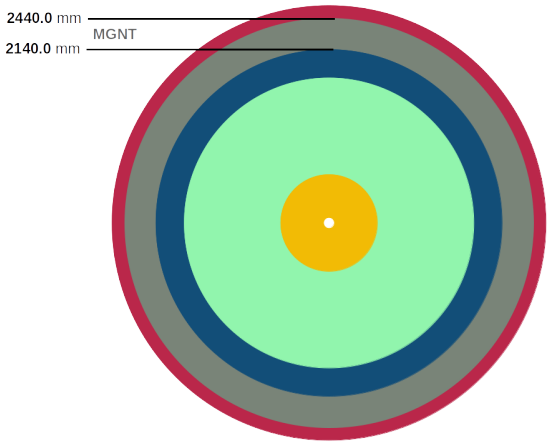

Figure 4.3: Illustration of the Magnet volume.

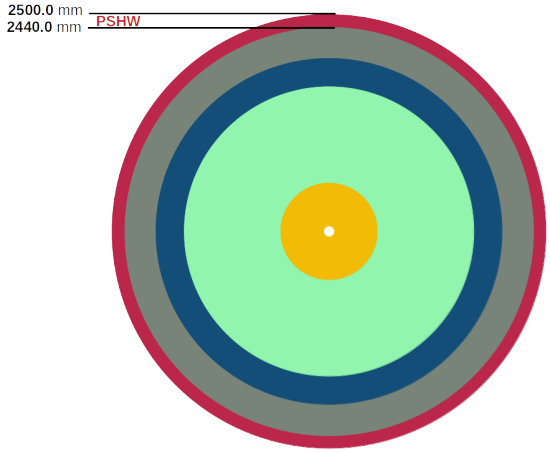

Figure 4.4: Illustration of the Preshower volume.

Preshower

The dimensions for the Preshower are (R_{in}= 2440 mm, R_{out}= 2500 mm). One active layer with inner radius = 2445 mm with thickness= 20 mm.

Figure 4.4 shows a drawing for the new volume for the Preshower.

Figures 4.5 is from the Geant4 simulation after the creation of the new volumes. As it appears there are two layers of the Si-Wrapper followed by one layer of magnet yoke, then one layer of the Preshower.

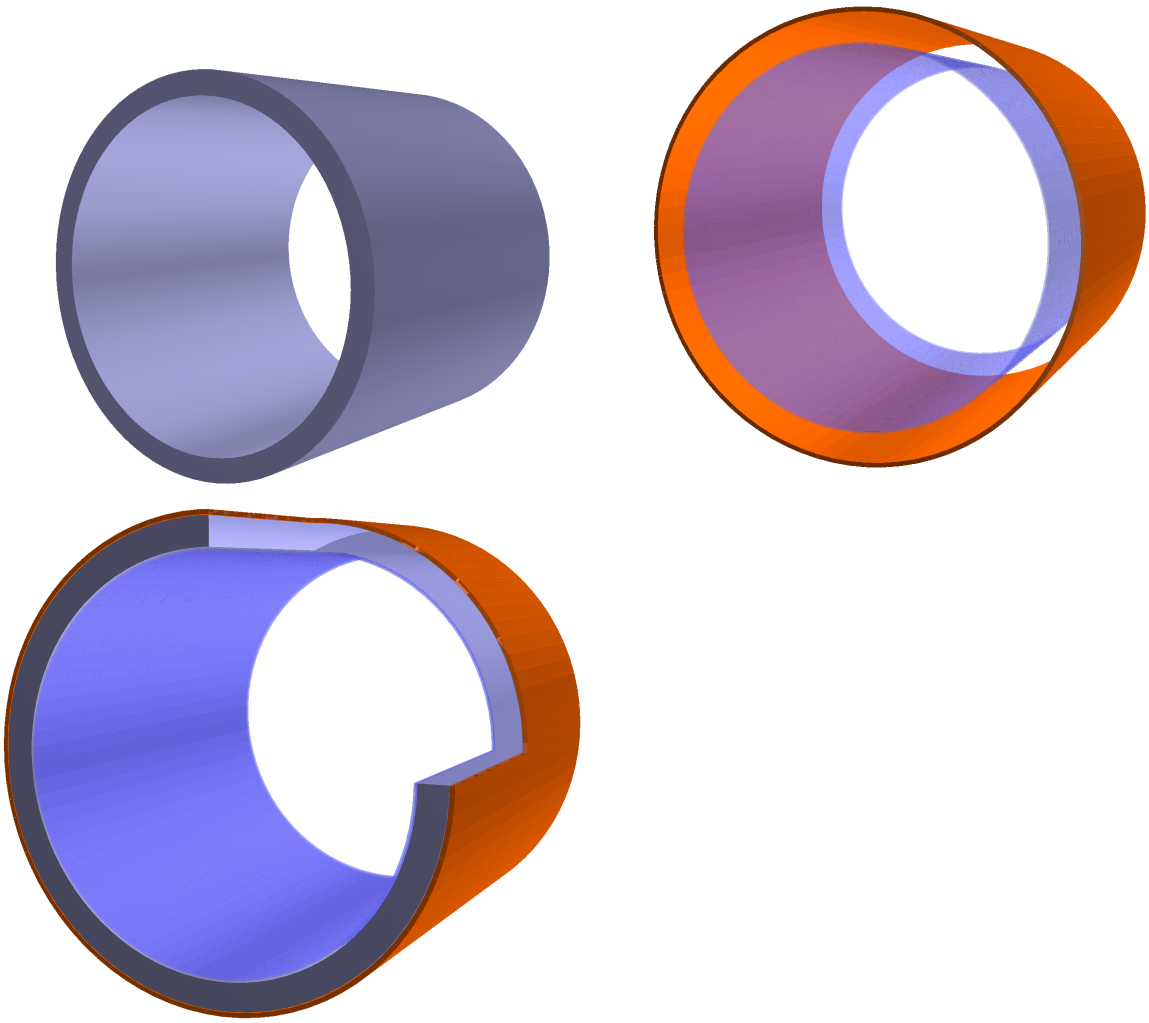

Figure 4.5: Geant4 visualization for Si-wapper, Magnet, and Preshower volumes. Top left: Magnet volume (in Cyan) as shown by Geant4 simulation. Top right: Si-Wrapper(in blue) and Preshower(in orange) volumes as shown by Geant4. Bottom left: Magnet, Si-Wrapper, and Preshower volumes as shown by Geant4.

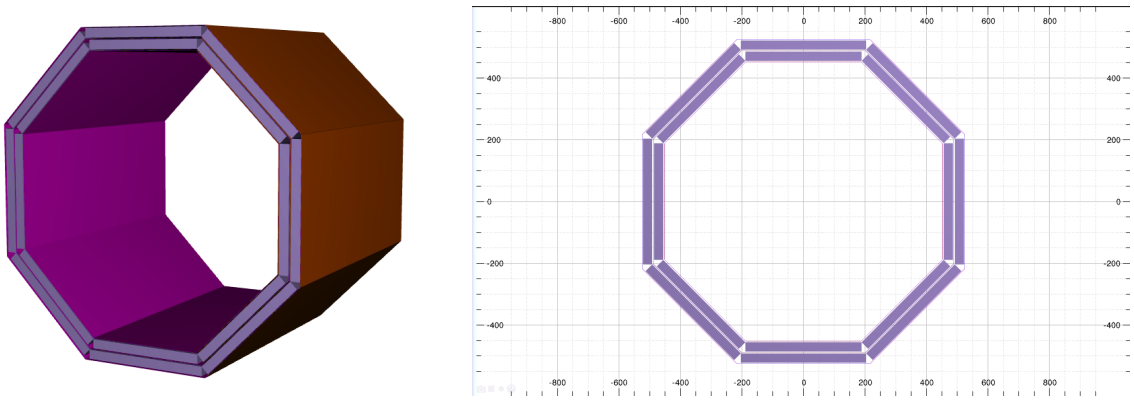

Figure 4.6: Geant4 visualization of the barrel muon system. Left: 3D view of the muon barrel system. Right: 2D section-view of the muon barrel system.

4.2.2 Implementation of the muon system sub-detector

The full description of the muon system has been done by defining the dimensions of the three muon detector stations and the two radiators. Furthermore, the description of the material of the μRWELL has been precisely described too.

The parameters of the muon system have been mentioned before in chapter 2, Table 2.8 contains the dimensions of the five stations that we have in our muon system. The current shape of the muon system takes the octagon form, which is still under study, and can be changed in the future.

Figure 4.6 shows the barrel part of the muon system visualization from Geant4.

Implementation of the μRWELL material

I have implemented the muon system materials depending on the material description of the μRWELL detector chambers. Table 4.1 shows the different layers materials of the μRWELL detector and it is going in order from top to bottom.

The properties of the copper and kapton materials are derived from the default GEANT4 libraries. The material termed Diamond-like-Carbon (DLC) has been introduced with a carbon density of $2.00\,\mathrm{g/cm^3}$. This same density is applied to represent the pre-preg layer, which serves as a film glue. FR_4, a composite material comprising 60% fiber glass and 40% epoxy, is characterized by densities of $1.99\,\mathrm{g/cm^3}$ and $1.25\,\mathrm{g/cm^3}$, respectively. In the simulation, it is treated as permaglass with a density of $1.85\,\mathrm{g/cm^3}$.

The gas mixture $ArCO_2CF_4$ is constructed using argon and CO_2 from the GEANT4 libraries, with respective densities of $1.661\,\mathrm{kg/m^3}$ and $1.842\,\mathrm{kg/m^3}$, along with CF_4, which is introduced as a new material with a density of $3.78\,\mathrm{kg/m^3}$. The densities of each component are adjusted based on their volume percentages (45% argon, 15% CO_2, and 40% CF_4), defined using fractional mass values: $f_{\mathrm{Ar}} = 0.295$, $f_{CO_2} = 0.109$, and

Table 4.1: Thickness and material of each layer of the μ-RWELL chamber implemented in GEANT4. Copper and kapton (in blue) description takes into account holes and dead zones on the amplification stage, while the copper in the readout PCB (red) accounts for strips. This table is taken from [50].

Component	Thickness of each layer	Material
	1.6 mm	FR_4
Cathode	35 μm	Copper
Gas gap	6 mm	$ArCO_2CF_4$
	5 μm	Copper
	50 μm	Kapton
	0.1 μm	DLC
μ-RWELL + readout PCB	35 μm	Copper
	100 μm	Film glue (same DLC density)
	35 μm	Copper
	1.6 mm	FR_4

$f_{CF_4} = 0.596$.

To account for the presence of holes and dead zones in the amplification stage, the densities of copper and kapton have been redefined. This redefinition involves assigning weights to distinguish active areas from dead areas on the amplification stage. The weight is determined by factors such as the shape, diameter, thickness, and pitch of the holes, as well as the size and pitch of the strips.

The final outcome of implementing a μ-RWELL chamber in GEANT4 is depicted in Figure 4.7.

4.2.3 Study of the Muon Track Deflection at IDEA

The muon track deflection at IDEA is a complex process that depends on a variety of factors, including the momentum of the muon, the type and thickness of the materials that the muon passes through, and the magnetic field in the IDEA detector.

Multiple scattering is the dominant process that causes muon track deflection at IDEA. Multiple scattering is a process in which a particle is deflected by a series of small-angle collisions with other particles. The amount of multiple scattering that a particle undergoes is proportional to the square root of the thickness of the material that the particle passes through and inversely proportional to the momentum of the particle.

The IDEA detector is a complex detector with a large number of components. Before reaching the muon system, muons must pass through all of the other subdetectors, including the tracking detector, the calorimeters, and the magnet coil.

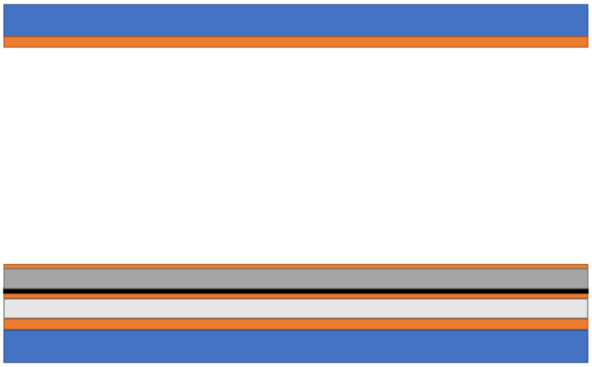

Figure 4.7: A schematic view of the various layers involved in the description of the μ-RWELL detector in GEANT4 is illustrated here. Starting from the top and proceeding to the bottom, these layers encompass: the cathode, the drift gap, filled with gas (depicted in white), the μ-RWELL structure adhered to the readout PCB, consisting of top copper and the kapton layer (representing the amplification stage) the DLC layer, a copper grid employed for charge evacuation, the pre-preg layer, Copper strips for readout, and the FR_4 layer. Figure is taken from [50].

The magnetic field in the IDEA detector also plays a role in muon track deflection. The magnetic field bends the trajectories of charged particles, including muons. The amount of bending depends on the strength of the magnetic field and the momentum of the particle.

Calculation of the effect of multiple scattering as a function of the momentum of muons caused by their interaction with the IDEA implemented material (all sub-detectors before the muon system) is crucial. This analysis aids in understanding the deviation of particle tracks and determining the required space resolution for the muon detector. These findings serve as valuable insights while developing our μRWELL detector. Steps involved in calculating the muon track deflection at IDEA:

- Identify all of the materials that the muon will pass through before reaching the muon system. This can be done by examining the geometry of the IDEA detector.
- Determine the thickness of each material. This information can be obtained from the engineering drawings of the IDEA detector.
- Calculate the multiple scattering angle for each material. This can be done using a variety of methods, such as the Bethe-Bloch formula.
- Sum the multiple scattering angles for all of the materials that the muon will pass through. This will give you the total muon track deflection.

Despite the challenges, it is important to calculate the muon track deflection at IDEA accurately. This information is used to design and optimize the muon system detector. Additionally, the muon track deflection is used to correct the trajectories of muons in the reconstruction of physics events. How the calculation of the muon track deflection at IDEA is used to develop the μRWELL detector:

The μRWELL detector is a type of muon chamber that is being developed for the IDEA detector. The μRWELL detector is designed to have a high spatial resolution, which is important for measuring the muon track deflection accurately.

The calculation of the muon track deflection at IDEA is used to optimize the design of the μRWELL detector. For example, the calculation is used to determine the size and spacing of the μRWELL detector strips.

The calculation of the muon track deflection at IDEA is also used to develop algorithms for reconstructing the trajectories of muons in the μRWELL detector. These algorithms are used to correct the muon trajectories for the effects of multiple scattering and the magnetic field.

Overall, the calculation of the muon track deflection at IDEA is an important tool for the design and development of the μRWELL detector.

I have written an algorithm to calculate the muon track deflection at IDEA environment to use it in Geant4 code. Figures 4.8 and 4.9 show examples for this deflection for two muons with different energies, 5 GeV and 50 Gev. As we can notice that the track deflection of the 5 GeV muon is much higher than the deflection of the 50 GeV muons, because the multiple scattering angle is inversely proportional to the momentum of the charged particle. This means that the lower the momentum of the particle, the larger the multiple scattering angle will be.

A full scan of the muon different energies starting from 5 GeV up to 50 GeV has been calculated, and the result is briefed in Figure 4.10.

The study of the track deflection as a function of the muon vertex is very important, since the muons can be produced at different vertices: Some of the muons are produced directly at the collision point, and others are produced by the decay of the other short lived particles produced from the collision. There are different sources of muons in our detector. Figure 4.11 shows the relation between the track deflection and the distance between the muon vertex and the muon system. As we can see from the deflection-distance relation, the deflection falls rapidly after distance = 2140 mm, which is the start of the magnet volume. At this distance the material density is much larger than before, because of the presence of the magnet, calorimeter's passive material, and muon system return yokes.

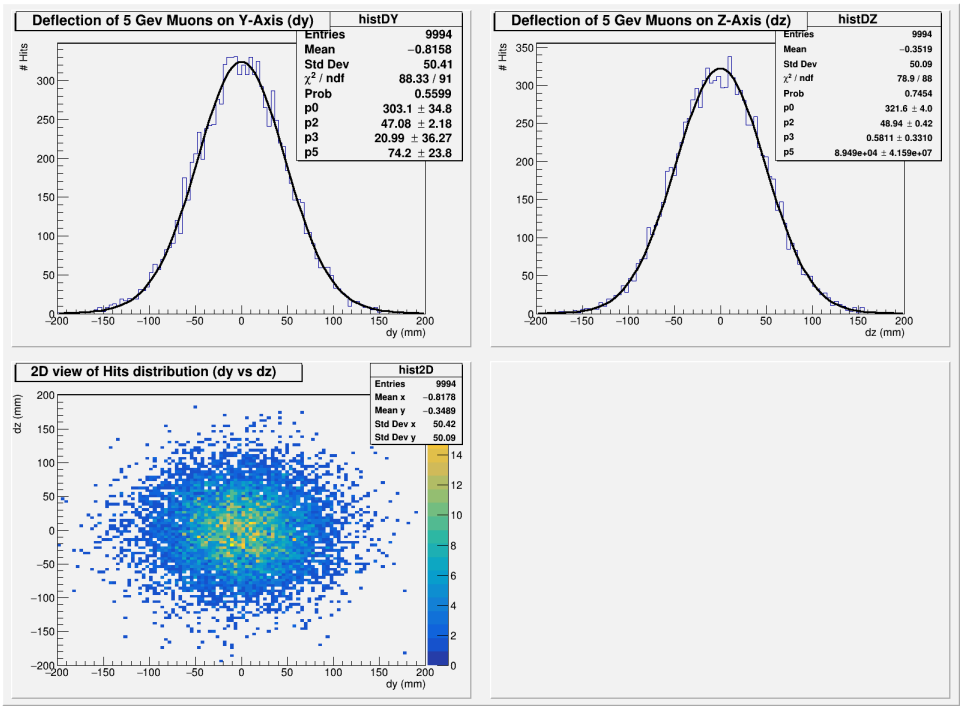

Figure 4.8: Track deflection of 5 GeV muons.

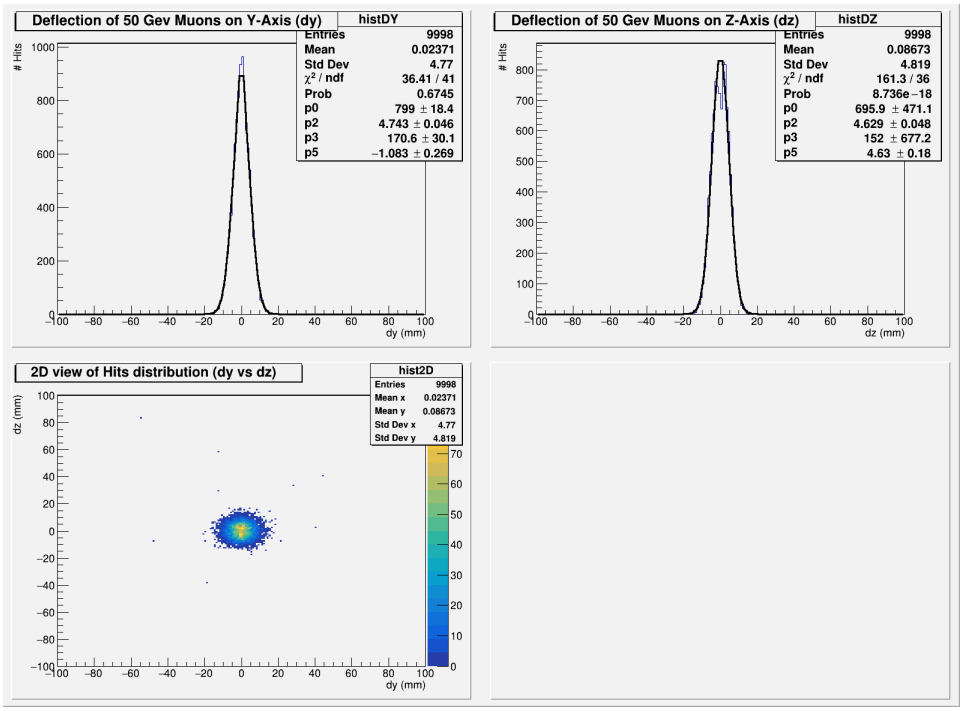

Figure 4.9: Track deflection of 50 GeV muons.

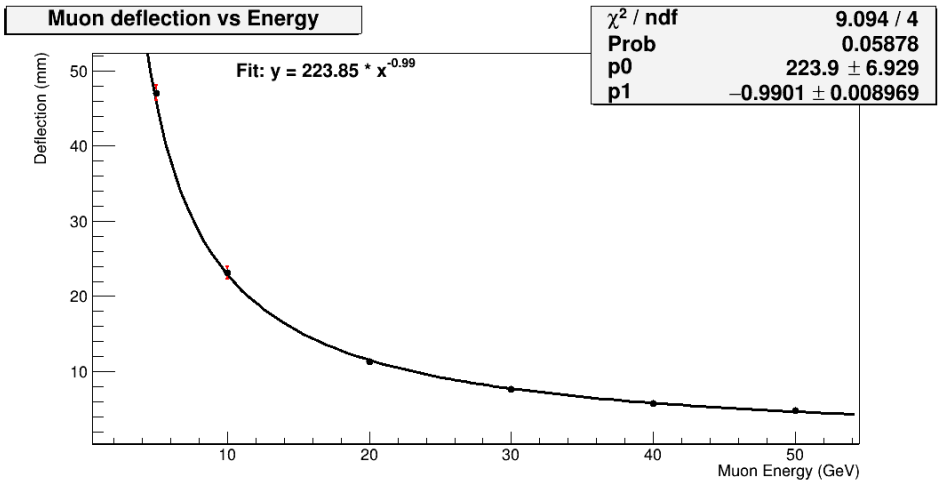

Figure 4.10: Muon track deflection as a function of muon energy.

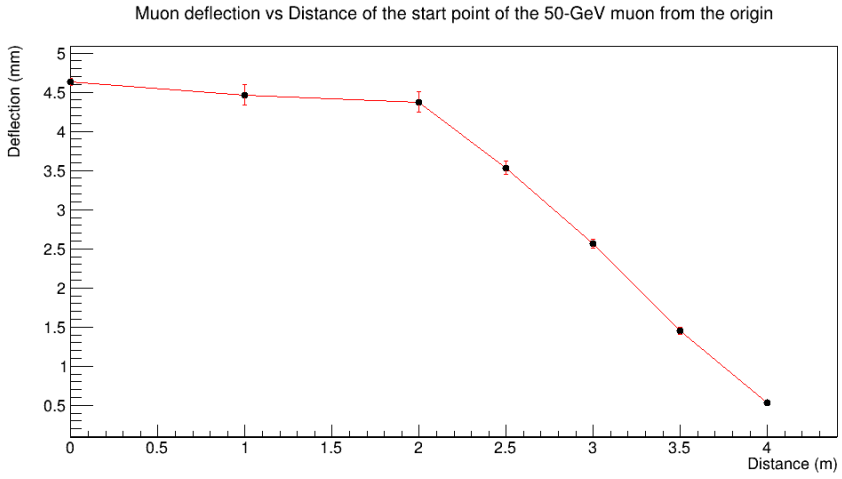

Figure 4.11: Muon track deflection as a function of the distance from its vertex.

Chapter 5

DD4HEP full simulation for IDEA muon system

5.1 DD4HEP Simulation Toolkit

DD4HEP (Detector Description for High Energy Physics) is a simulation toolkit [51] for high energy physics experiments. It is a generic toolkit that can be used to describe a wide range of detectors, from simple tracking detectors to complex calorimeters. DD4HEP is based on the ROOT geometry package, but it provides a number of additional features and interfaces that make it easier to use for detector simulation.

One of the key features of DD4HEP is its ability to generate realistic detector geometries. DD4HEP can be used to generate geometries that are based on CAD drawings or on analytical descriptions. DD4HEP also supports a variety of geometric primitives, such as volumes, surfaces, and materials.

Another key feature of DD4HEP is its integration with Geant4. DD4HEP can be used to generate Geant4 geometries automatically, which simplifies the setup of Geant4 simulations.

DD4HEP is a powerful and flexible toolkit for detector simulation. It is used by a number of high energy physics experiments, including the LHCb and the CMS experiments at the LHC.

5.1.1 Key Features

DD4HEP offers several key features and capabilities that make it a valuable resource for the HEP community:

- **Modular Design:** DD4HEP is built on a modular architecture, allowing users to assemble detector geometries from reusable components. This modularity simplifies the description of complex detectors and promotes code reusability.

- **Geometry Description:** The toolkit provides a framework for defining detector geometries, including the placement and orientation of detector elements. This information is crucial for accurate simulation and event reconstruction.
- **Visualization:** DD4HEP includes visualization tools that enable users to interactively view and manipulate detector geometries. Visualization aids in detector design, validation, and understanding.
- **Detector Simulation:** DD4HEP can interface with popular Monte Carlo simulation engines, such as Geant4, to perform detailed particle transport and interaction simulations within the defined detector geometries.
- **Data Output:** The toolkit supports various output formats, including ROOT and XML, allowing users to store and analyze simulated data efficiently.

5.1.2 Toolkit design

The core element of DD4hep is the so-called Generic Detector Description Model (GDDM). Figure 5.1 depicts the interaction of the main components of DD4hep and their interfaces to the end-user applications, namely the simulation, reconstruction, alignment, and visualization. The generic detector description is an in-memory model, consisting of a set of objects containing geometry and auxiliary information about the detector. It is envisioned that the GDDM can be constructed through several means, but the current development is focused on a mechanism that converts a compact detector description in XML format through specialized code fragments (called Detector constructors) into the GDDM. These code fragments instantiate the GDDM of the detector defined by a set of C++ classes. From this model, it is possible to transform the GDDM in memory to, for example, Geant4 geometry or a GDML file.

The compact detector description

The compact description, in its minimalistic form, may not suffice in the later stages of the detector's lifecycle and is likely to be replaced or refined when a more realistic detector with deviations from the ideal is required by the experiment.

In the compact description, the detector is parametrized in minimalistic terms with user-provided parameters in XML. XML is an open format, and the DD4hep parsers do not validate against a fixed schema, thus allowing for the easy introduction of new elements and attributes to describe detectors. This feature minimizes the burden on the end-user while still providing flexibility.

The nature of the compact description, which aims to use as little information as necessary to describe the detector, implies that the interpretation of this information is

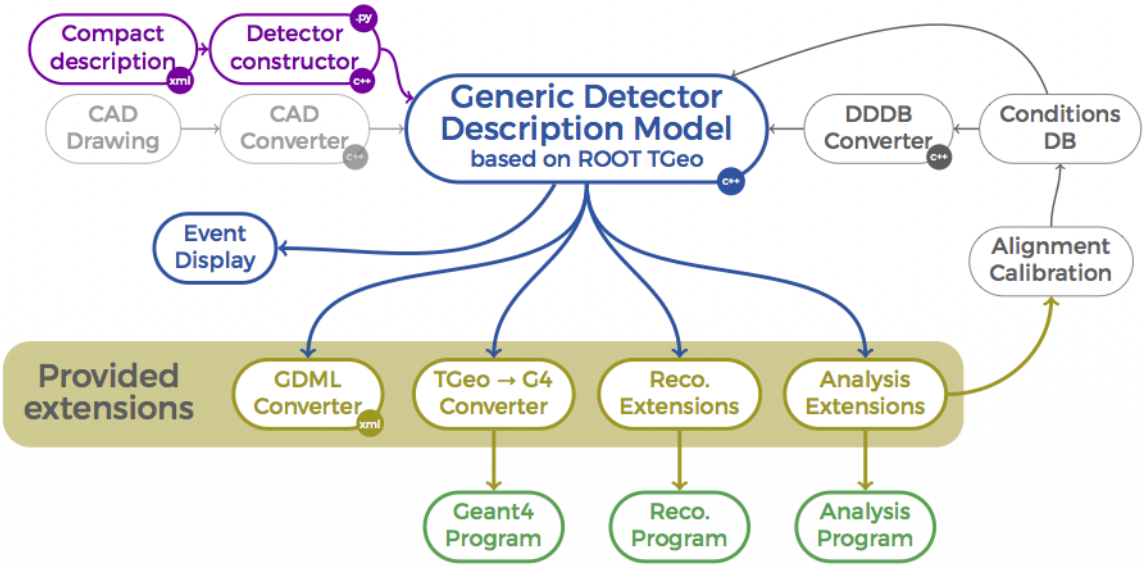

Figure 5.1: The components of the DD4hep detector geometry toolkit. This image is taken from [52].

performed by specialized code fragments, known as Detector Constructors, described in the following section.

Detector Constructors

Detector Constructors are relatively small code fragments that take, as input, an XML element from the compact description, representing a single detector instance. The code interprets the data and expands its geometry model in memory using the elements from the generic detector description model described in the following section. The toolkit invokes these code fragments in a data-driven way using naming conventions during the initialization phase of the application. Users focus on one single detector type at a time, but the toolkit supports them in constructing complex and large detector setups. Two implementations are currently supported: one is based on C++, which performs better and can detect errors at compile time, while the other is based on Python fragments where the code is more readable and compact, but errors are only detected at execution time.

The compact description, together with the detector constructors, is sufficient to build the detector model and visualize it. If, during the lifetime of the experiment, the detector model changes, the corresponding constructors will need to be adapted accordingly. DD4hep already provides a palette of basic pre-implemented geometrical detector concepts to design experiments. In view of the usage of DD4hep as a detector description toolkit, this library may, in the future, also adopt generic designs of detector components

created by end users, for example, during the design phase of future experiments.

GDDM

The aim of the GDDM is to build an in-memory model of the detector that can provide geometrical as well as functional facets. It is based on the TGeo geometry package from ROOT with certain extensions. The TGeo geometry classes are used directly without isolation interfaces, with the exception of detector constructors, where users can write easy, compact, and readable code for custom detector constructors. The in-memory object is structured as a tree of DetectorElement objects. These elements provide an easy entry point to any given detector part of the apparatus and represent a complete sub-detector (e.g., tracker or calorimeter), a part of a sub-detector (e.g., tracker-disk or tracker-barrel), a module, or any other arbitrary sub-detector part. The main purpose is to provide easy access to desired sub-detector information. If a tracking program wants access to the tracker DetectorElement, DD4hep will allow the program access to all the geometry properties, alignment and calibration constants, and other slowly varying conditions such as temperatures. The DetectorElement acts as a data container. DD4hep provides a singleton object called Detector, through which access to the whole geometry is possible, and which provides, at the same time, ownership, bookkeeping, and management properties to the instances of the detector model.

As shown in Figure 5.2, an application might require special functionality. This can be achieved with specialized classes that extend the DetectorElement. Such extensions are usually needed in addressing issues connected to reconstruction algorithms, such as pattern recognition, tracking, vertexing, and particle identification. One example could be surfaces that aid in track fitting. A generic detector description toolkit cannot address all cases, as there are far too many of them, but it can provide a flexible extension mechanism via code fragments to develop the necessary functionality needed for a given case. Depending on the case, the extensions can store additional specialized data, expose additional behavior, or both. The user can easily add additional behavior by overloading the DetectorElement class and extending its internal data. Since the internal data is public and addressed by reference, an arbitrary number of extensions can be created with minimal overhead. In addition to this, more data can be incorporated at any time by the user into this scheme by using a simple aggregation mechanism. The only constraint is that these data extensions have to be of different types. It is thus possible to optimize the attachment depending on the particular use case. DD4hep utilizes this functionality in the reconstructions extension called DDRec.

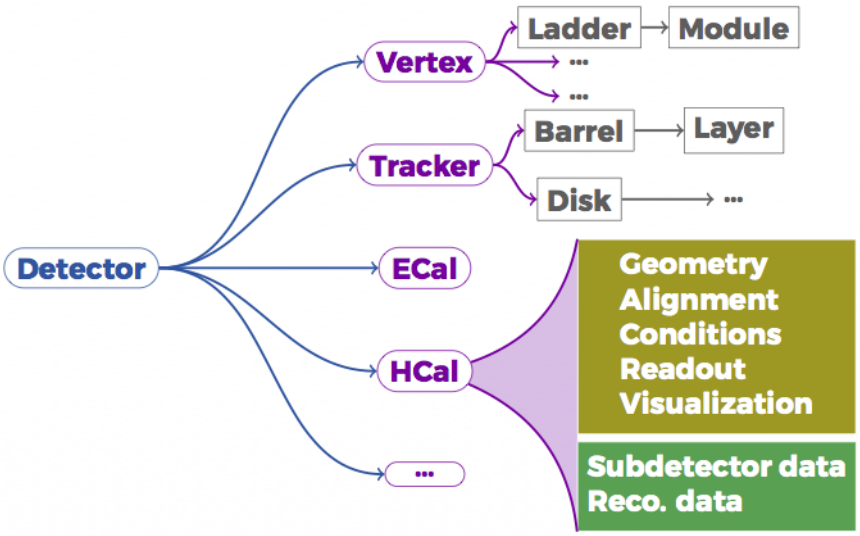

Figure 5.2: The tree structure of DetectorElement objects that constitute the GDDM. This image is taken from [52].

5.2 Full simulation of IDEA muon system

The FCC collaboration has decided to use KEY4HEP toolkit -which DD4HEP is part of its framework- in the simulation and analysis of all the experiments included within the collaboration. So, in our case as IDEA detector simulation, I used DD4HEP to describe our muon detector geometry.

The implementation of the muon system in DD4HEP in my master thesis work have been through two tracks:

1. As a first approach as a simple cylindrical shaped, which describe the muon system as layers of cylinders contains the different materials of our detector.

2. Then gradually a description of complicated and detailed muon system, which describe the mosaics of 50 $\times$ 50 cm^2 detailed μRWELL chambers.

5.2.1 Simple cylindrical shape

The advantage of a simple description approach is to provide us with:

- A functional version in a short time, facilitating numerous pertinent physics investigations.

- It offers great adaptability, considering that the muon chamber, being the final detector in the sequence, is susceptible to adjustments necessitated by alterations in other sub-detectors.

As it previously stated in last section about the DD4HEP toolkit, in order to describe and simulate the detector in DD4HEP, we need to write a detector constructor and a compact description. In this section I shall describe the detector constructor and the compact description for the simple cylindrical shape of the muon system.

The detector constructor

The provided code exemplifies a fundamental aspect of DD4HEP. Detector constructors within DD4HEP serve as essential components for building and configuring complex particle detectors. In the presented code, I created a detector constructor named **SimpleSensitiveLayeredCylinder_o1_v00**, showcasing the core principles of DD4HEP's detector modeling capabilities.

My detector builder creates a factory for a shape from multiple cylinders, among theses cylinders you can specify the sensitive and non-sensitive layers of them.

At its core, DD4HEP's detector constructors are responsible for interpreting user-defined detector specifications, often provided in XML format, and translating them into a detailed, in-memory representation of the detector. In this case, the constructor takes three input arguments: a reference to the overarching `dd4hep::Detector` object (`lcdd`), a handle to an XML element (`xmlElement`), and an instance of `dd4hep::SensitiveDetector` (`sensDet`). These arguments collectively enable the construction of a layered cylinder-shaped detector. These arguments are described in the following part of code:

```
static dd4hep::Ref_t createSimpleSensitiveLayeredCylinder_o1_v00(dd4hep
    ::Detector& lcdd,
        dd4hep::xml::Handle_t xmlElement,
        dd4hep::SensitiveDetector sensDet)
```

The code proceeds to extract information from the XML element, defining the dimensions, materials, and properties of the detector layers. It then iterates over child elements, creating individual layers of the detector with specified characteristics. Importantly, it allows for the design of sensitive layers capable of detecting particles, as well as configuring their sensitivity properties. Visualization attributes, such as color and style, can also be defined to aid in visualizing the detector. The following part of code shows how to build the layers in iteration way:

```
  // Create layer cylinders with their respective material, etc
  auto layers = xmlElement.children(_Unicode(layer));
  auto numLayers = xmlElement.numChildren(_Unicode(layer), true);
  int sensitiveLayerIndex = 0;
  dd4hep::xml::Handle_t layer(layers.reset());
  for (unsigned layerIdx = 0; layerIdx < numLayers; ++layerIdx) {
    dd4hep::xml::DetElement layerDet = static_cast<dd4hep::xml::
   DetElement>(layer);
    dd4hep::Tube layerShape(layerDet.rmin(), layerDet.rmax(), layerDet.
   dz());
```

```
    std::string layerName = dd4hep::xml::_toString(layerIdx, "layer%d")
    ;
```

Depending on the last line of the previous part of code, the builder will create a new cylinder every time a layer will be created in the XML file. Where the following part is the responsible for determining the sensitivity of the layer:

```
    if (layer.hasAttr("sensitive") && layerDet.isSensitive()) {

      dd4hep::xml::Dimension sdType(xmlElement.child(_U(sensitive)));//
    if called outside of the loop it breaks existing configs without
   sensitive layers
      sensDet.setType(sdType.typeStr());
      layerVolume.setSensitiveDetector(sensDet);
      layerPlacedVolume.addPhysVolID("layer", sensitiveLayerIndex);
      sensitiveLayerIndex++; }
```

The word *layer* in this case has to be mentioned in the bit field, where we define the number of bits to save the data from the readouts.

DD4HEP encourages a hierarchical approach to detector modeling, allowing the construction of sub-detectors within a larger apparatus. The detector constructors offer the flexibility to adapt to dynamic changes in the detector's configuration, making them indispensable for evolving experiments.

DD4HEP supports multiple programming languages for detector constructors, including C++ and Python, providing a balance between performance and code readability. Additionally, the toolkit promotes code reusability by offering a library of pre-implemented geometrical detector concepts while allowing users to extend functionality as needed.

In summary, the presented code snippet is a testament to DD4HEP's capabilities in constructing intricate particle detectors, enabling physicists to define, simulate, and visualize complex detector models for high-energy physics experiments. The expected XML structure (the 'sensitive' keyword is optional and default to false):

```
<detector type="SimpleSensitiveLayeredCylinder_o1_v00" ...>
<dimensions rmin="..." rmax="..." dz="..." z_offset="...">
<sensitive type="SimpleTrackerSD"/>
<layer rmin="..." rmax="..." dz="..." z_offset="..." material="...">
...
<layer rmin="..." rmax="..." dz="..." z_offset="..." material="..."
 sensitive="true">
</detector>
```

The compact description

My XML code defines parameters, readouts, and detectors for a Muon System. This Muon System is divided into two main sections: the Barrel and the Endcap. Each section

is further divided into multiple layers, each having specific materials and dimensions. Below is a detailed description of the XML code:

Constants: The XML code begins with the definition of various constants used in the Muon System. These constants specify parameters such as radii, thicknesses, and lengths of different components of the system. Notable constants include the inner and outer radii of the Barrel and Endcap, as well as the thicknesses of various detector layers.

Readouts: The XML code defines readout configurations for different parts of the Muon System. Three readout configurations are specified: **MuonChamberBarrelReadout**, **MuonChamberPositiveEndcapReadout**, and **MuonChamberNegativeEndcapReadout**. Each readout is characterized by the number of ϕ and θ bins for segmentation.

Detectors: The XML code defines the detectors for the Muon System, including the MuonBarrel and MuonPositiveEndcap. These detectors are composed of multiple layers, each with specific materials and dimensions. Each layer is described individually, and the following properties are specified for each layer:

- **dimensions**: Specifies the dimensions of the envelope, including the radial boundaries (rmin and rmax), half-length (dz), and z-offset.
- **sensitive**: Indicates whether the layer is sensitive to interactions (true or false).
- **material**: Specifies the material composition of the layer.
- **vis**: Defines the visualization properties of the layer.
- **color**: Specifies the color of the layer (if applicable).

The layers in each detector represent different components such as G10_FR4 layers, copper layers, gas layers, Kapton layers, Carbon Fiber layers, and Silicon layers. Additionally, there are return yoke layers made of iron.

Our goal is to make the code flexible as much as possible, so it can be easily editable for the user. I did the same in the XML file that describes the simple version, it is almost automated, in which the user only edits the main parameters at the beginning of the XML, and the code adjusts the changes automatically to build the sensitive cylindrical layers. The following part of XML shows the main parameters of the muon barrel system that can be also changed by the user later, while the description of the detector itself doesn't contain numbers. That makes the code almost automated and controlled by some parameters.

```
1              <!---   Muon System Parameters    -->
2    <constant name = "BarrelInnerRadius"          value = "4500*mm"/>
3    <constant name = "BarrelOuterRadius"          value = "5280*mm"/>
4    <constant name = "BarrelFirstLayerRadius"     value = "4520*mm"/>
5    <constant name = "BarrelFirstYokeRadius"      value = "4560*mm"/>
```

```
    <constant name = "BarrelSecondLayerRadius"      value = "4880*mm"/>
    <constant name = "BarrelSecondYokeRadius"       value = "4920*mm"/>
    <constant name = "BarrelThirdLayerRadius"       value = "5240*mm"/>
    <constant name = "BarrelLength"                 value = "9000*mm"/>
    <constant name = "BarrelThirdLayerLength"       value = "10520*mm"/>
```

At the same time the parameters of the μRWELL chambers can be defined too, the following values describe the chamber that we have right now, which would have some changes in the future.

```
        <!--    microRWELL chamber different layers thicknesses    -->
    <constant name = "G10_FR4Thick"                 value = "1.6*mm"/>
    <constant name = "CuThick"                      value = "0.035*mm"/>
    <constant name = "GasLayerThick"                value = "6*mm"/>
    <constant name = "Cu2Thick"                     value = "0.005*mm"/>
    <constant name = "KaptonThick"                  value = "0.05*mm"/>
    <constant name = "CarbonFiberThick"            value = "0.0001*mm"/>
    <constant name = "CarbonFiber2Thick"            value = "0.1*mm"/>
    <constant name = "SiThick"                      value = "1.6*mm"/>

        <!--   Return yoke thickness    -->
    <constant name = "YokeThick"                     value = "300*mm"/>
```

One of the most important part of the detector description is the readout, where we can define the segmentation of our detector with describing cell size. The readout system is often used to collect data from sensors or detectors.

```
  <readouts>
    <readout name="MuonChamberBarrelReadout">
      <segmentation type="ProjectiveCylinder" phi_bins="3066"
   theta_bins="900"/>   <!-- Depending on cell size 1cm*1cm  -->
      <id>system:4,layer:2,theta:10,phi:-12</id>
    </readout>
```

Detector visualization

DD4HEP can produce an output to be visualized by ROOT. The following figures shows our muon system described by DD4HEP and visualized by ROOT.

5.2.2 Detailed version of the muon system

The aim of the detailed version is to have a simulation of the muon system as much similar as to the real version that will be built in the experiment.

The detailed version of the muon system is under construction now, with the goals:

- Building the muon system based on $50 \times 50\ cm^2$ μRWELL chambers.

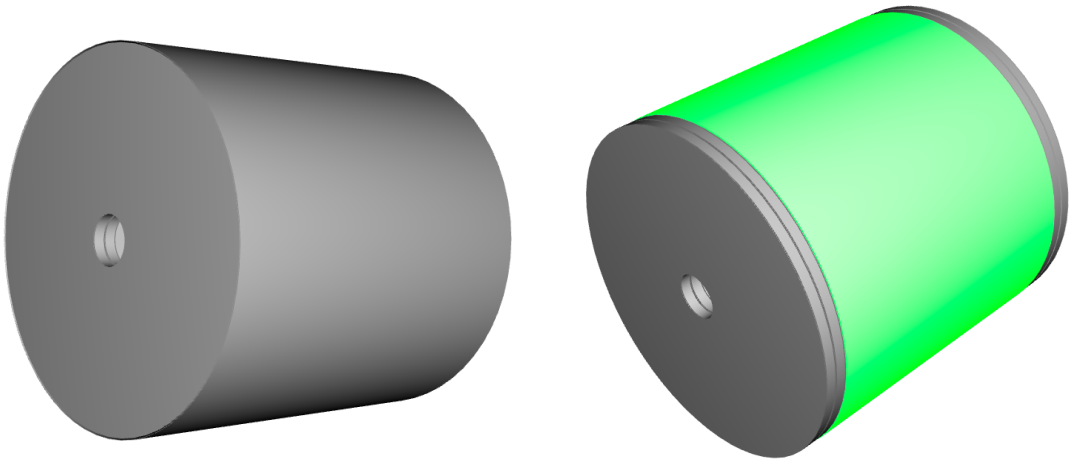

Figure 5.3: Muon system (Barrel+Endcap). Left: Full Muon system. Right: Muon system without the last detector barrel station.

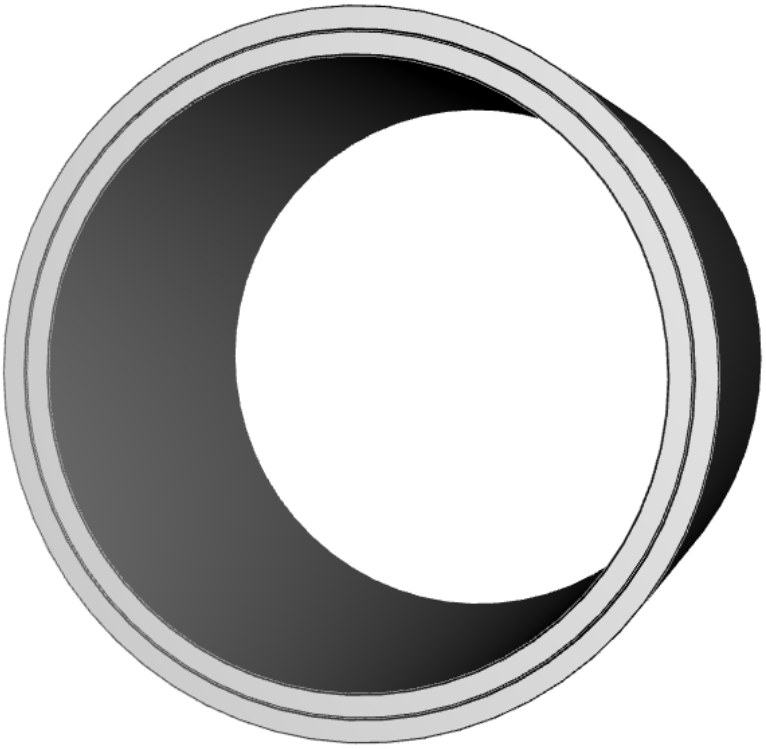

Figure 5.4: Cross-section of the muon barrel system.

- Taking into account the overlap between the chambers in 2 dimensions (to minimize the dead area as much as possible).
- Making the design flexible, where the user can choose the number of sides of the shape (hexagon, octagon, ...), and automatically the builder will calculate the number and places of the copied chambers.
- If the side length do not fit with an integer number of 50×50 cm^2, the builder can make a chamber with unusual dimensions, which can fit the excess area at the end of the side (the R&D group makes this option available in manufacturing too).

Figure 5.5: Overlap in 1 direction.

5.2.3 Simulating the hits in the muon system

Gaudi framework

I used DD4HEP to describe the geometry of the muon detector. This information can then be used to simulate the interactions of particles with the detector. DD4HEP can also be used to generate Geant4 geometries automatically, which simplifies the setup of Geant4 simulations.

On the other hand, **Gaudi** provides a framework for building and running HEP applications, which is a part of the KEY4HEP framework too. It includes a variety of features, such as event management, data handling, and visualization. Gaudi can be used to build applications for a variety of tasks, including simulation, reconstruction, and analysis.

The relationship between DD4HEP and Gaudi is that DD4HEP can be used to generate the Geant4 geometry for a Gaudi-based simulation. This allows users to take advantage of the features of both toolkits.

To simulate hits in DD4HEP and Gaudi, you would first need to create a Geant4 geometry of the detector. This can be done using DD4HEP or another tool. Once you have the Geant4 geometry, you can use a Geant4 simulation to simulate the interactions of particles with the detector. The Geant4 simulation will generate hits on the detector surfaces.

To simulate hits in Gaudi, you need to use the Gaudi simulation framework. The Gaudi simulation framework will create Gaudi hits from the Geant4 hits. The Gaudi hits can then be used for reconstruction and analysis.

Linking our muon system with Gaudi

I have simulated the hits produced in our simple cylindrical-shaped muon system in Gaudi and got the following results.

Figure 5.6 shows 100 muons each with momentum 10 GeV, simulated through our muon system, as we can see the position of the hits in the sensitive areas in our detector.

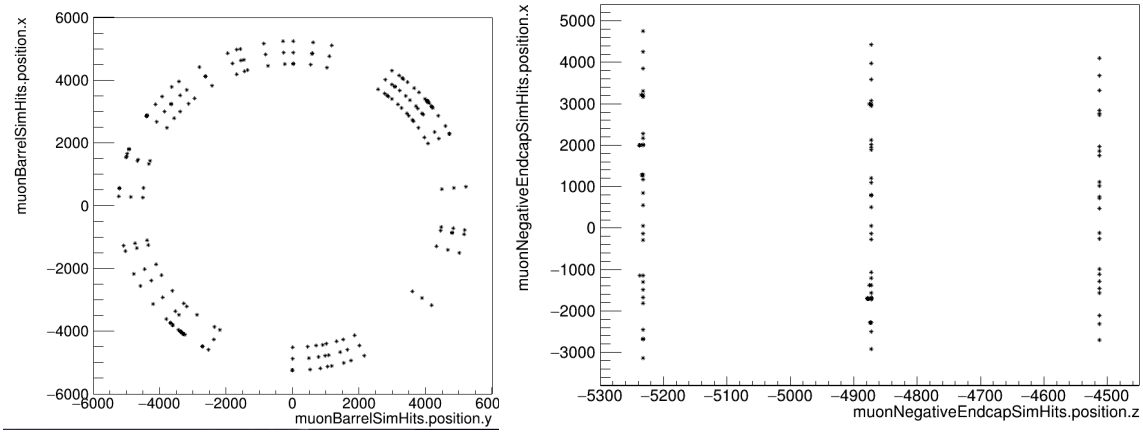

Figure 5.6: Hits from the muon system. Left: Hits from the bareel muon system. Right: Hits from one of the endcap muon system.

Calculation of the Material Budget of the muon system

The material budget of a detector is a measurement of the amount of material that a particle must traverse in order to pass through the detector. It is expressed in units of radiation length (X_0). The radiation length is a measurement of the distance that a high-energy electron will travel before losing 90% of its energy due to bremsstrahlung.

To calculate the material budget of a detector, you must first identify all of the materials that the particle will traverse. Once you have identified the materials, you need to know the thickness of each material. The material budget can then be calculated using the following formula:

$$\text{Material budget} = \sum_{i=1}^{N} \left(\text{thickness}_i \cdot X_0^i\right) \tag{5.1}$$

where:

- N is the number of materials traversed by the particle
- $thickness_i$ is the thickness of material i
- X_0^i is the radiation length of material i

The material budget is an important quantity to consider when designing and operating a detector. A high material budget can lead to multiple scattering and energy loss, which can degrade the performance of the detector. It is important to design detectors with a material budget that is low enough to meet the performance requirements of the experiment.

In KEY4HEP, the calculation of the material budget can be calculated easily through Gaudi; figure 5.7 shows the material budget of our simple cylindrical-shaped muon system.

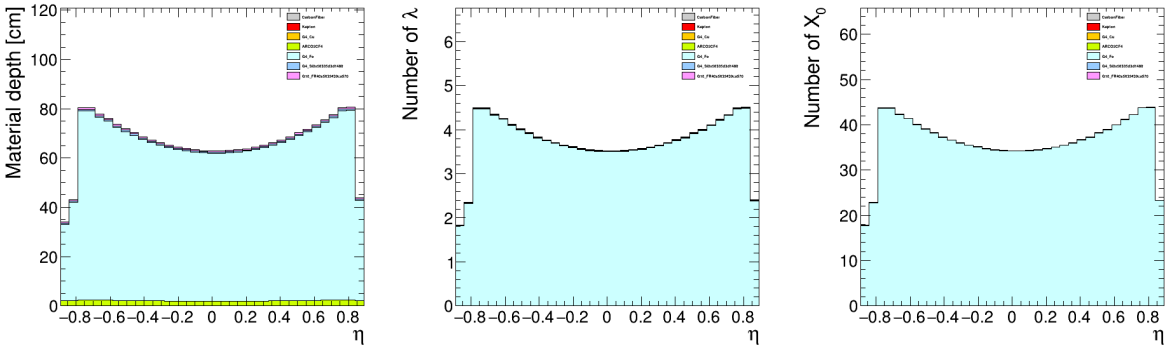

Figure 5.7: Material budget of the muon system. Left: The depth of the material. Middle: # of interaction lengths. Right: # of radiation lengths.

Chapter 6

Conclusion

In the pursuit of advancing the field of high-energy particle physics, this thesis has explored the development of the μRWELL detector technology, its simulation, and visualization into the IDEA detector concept. Particle detectors play a pivotal role in unraveling the mysteries of the universe by enabling the detection and characterization of subatomic particles. The discussions within this thesis have encompassed key topics, ranging from the fundamental principles underlying particle detection to the practical implementation of detector technologies.

Simulation emerged as a critical tool in the development and optimization of particle detectors. Geant4 and DD4HEP, among other simulation frameworks, were explored, shedding light on their capabilities in simulating particle interactions and the detector response. Through simulation, researchers can test and refine detector designs, predict experimental outcomes, and optimize performance.

In this master's thesis, the work has been undertaken in two complementary sectors:

1. Development of a full simulation of the muon detection system within the IDEA experimental apparatus. The simulation encompasses the interaction of muons with the detector, as well as the digitization of the electronic signals generated within the detectors.

2. Concurrently, work is conducted in the hardware domain, focusing on detector R&D. This involves the development and testing of the μRWELL technology both in the laboratories at Bologna and CERN.

The main results obtained in the thesis work, which demonstrate scientific relevance and originality, can be outlined as follows:

- The successful implementation of the muon system and preshower geometries and materials definition in Geant4 simulation. Additionally, accurately describes the

muon system in DD4HEP simulation toolkit and links it with Gaudi for simulating the hits.

- Calculation of the material budget for the IDEA detector. The development of a dedicated code to calculate the material budget of the entire IDEA detector is a valuable contribution. By writing a code to determine the number of radiation lengths in each sub-detector, this code enables us to analyze the energy loss and scattering of particles as they traverse different detector materials. The calculated material budget for each sub-detector separately further enhances the precision and applicability of the results.

- The calculation of the effect of multiple scattering as a function of the momentum of muons caused by their interaction with the implemented material is crucial. This analysis aids in understanding the deviation of particle tracks and determining the required space resolution for muon detectors. These findings serve as valuable insights while developing our μRWELL detector.

- In the hardware aspect, I actively took part in two test beam activities conducted at CERN during June 2023 and August 2023 to assess our detector proposals. Through collaborative efforts with the RD-FCC group in Bologna, along with Ferrara and LNF at Frascati, we developed two different 2D layout configurations for μRWELL detectors. These detectors underwent rigorous testing using high-energy beams at CERN, utilizing various high voltages, with the goal of determining the optimal layout for integration into the IDEA experiment. The preliminary results obtained with the 2D layout are very promising and encouraging, with a spatial resolution of 200 μm for the muon system and < 100 μm for the preshower.

As the curtain falls on this chapter, our contributions echo through the corridors of particle physics, paving the way for future explorations into the unknown. This thesis encapsulates not just our journey but also the shared aspirations of scientists striving to unravel the universe's deepest secrets. With every simulation, every experiment, and every discovery, we inch closer to understanding the profound mysteries that have eluded us for so long.

Bibliography

[1] M. Benedikt et al. "Future Circular Collider Study. Volume 2: The Lepton Collider (FCC-ee) Conceptual Design Report". In: *Eur. Phys. J. ST* CERN accelerator reports.CERN-ACC-2018-0057 (2018).

[2] B. Richter. "Nucl. Instr. Methods". In: 136 (1976), p. 47.

[3] CEPC-SPPC Study Group. *CEPC-SPPC Preliminary Conceptual Design Report. 1. Physics and Detector*. Technical Report IHEP-CEPC-DR-2015-01. IHEP-TH-2015-01, IHEP-EP-201501. IHEP, 2015.

[4] T. Behnke et al. "The International Linear Collider Technical Design Report – Volume 1: Executive Summary". In: (2013). arXiv: arXiv:1306.6327 [physics.acc-ph].

[5] M. Aicheler et al. *A Multi-TeV Linear Collider Based on CLIC Technology*. CERN Yellow Reports: Monographs. CERN, Geneva, Switzerland, 2012. URL: https://cds.cern.ch/record/1500095.

[6] CEPC Study Group. "CEPC Conceptual Design Report". In: IHEP-CEPC-DR-2018-01, IHEP-AC-2018-01 (2018). arXiv: 1809.00285 [physics.acc-ph].

[7] K. Fujii et al. "Physics Case for the 250 GeV Stage of the International Linear Collider". In: (2017). arXiv: 1710.07621 [hep-ex].

[8] CLICdp, CLIC Collaboration, and M.J. Boland et al. "Updated baseline for a staged Compact Linear Collider". In: (2016). DOI: 10.5170/CERN-2016-004.

[9] A. Apollonio et al. "FCC-ee operation model, availability, and performance". In: *Proceedings of ICFA Advanced Beam Dynamics Workshop eeFACT2018*. Hong Kong, 2008.

[10] N. Bacchetta et al. "CLD – A Detector Concept for the FCC-ee". In: (Nov. 2019). arXiv: 1911.12230 [physics.ins-det].

[11] Gabriella Gaudio. "The IDEA detector concept for FCCee". In: *PoS* ICHEP2022 (Nov. 2022), p. 337. DOI: 10.22323/1.414.0337.

[12] Alain Blondel and Frank Zimmermann. "A High Luminosity e^+e^- Collider in the LHC tunnel to study the Higgs Boson". In: (Dec. 2011). arXiv: 1112.2518 [hep-ex].

[13] The LEP Electroweak Working Group et al. In: *Physics Reports* 427 (2006), p. 257.

[14] The LEP Electroweak Working Group and the ALEPH DELPHI L3 OPAL Collaborations. In: *Physics Reports* 532 (2013), p. 119.

[15] M. J. G. Veltman. "Limit on Mass Differences in the Weinberg Model". In: *Nucl. Phys. B* 123 (1977), pp. 89–99. DOI: 10.1016/0550-3213(77)90342-X.

[16] *Future Circular Collider Study. Volume 1: Physics Opportunities. Conceptual Design Report*. Tech. rep. CERN-ACC-2018-0056. Published in Eur. Phys. J. C. Geneva: CERN accelerator reports, 2018.

[17] J. Haller et al. "Update of the Global Electroweak Fit and Constraints on Two-Higgs-Doublet Models". In: *arXiv preprint arXiv:1803.01853* (2018). arXiv: 1803.01853 [hep-ph].

[18] A. Hoecker. *Private Communication*. Presentation: https://indico.cern.ch/event/716380/contributions/2944841/attachments/1660046/2660284/epfaculty-hoecker-1jun2018.pdf. 2018.

[19] P. Azzi et al. "Prospective Studies for LEP3 with the CMS detector". In: *arXiv:1208.1662 [hep-ex]* (2012). Preprint CMS-NOTE-2012-003.

[20] M. E. Peskin. "Comparison of LHC and ILC capabilities for Higgs boson coupling measurements". In: *arXiv preprint arXiv:1207.2516* (2012).

[21] I. Esteban et al. "JHEP 1, 87 (2017)". In: *Journal of High Energy Physics* 1 (2017), p. 87. DOI: 10.1007/JHEP01(2017)087.

[22] R.N. Mohapatra. "Phys. Rev. Lett. 56, 561 (1986)". In: *Physical Review Letters* 56 (1986), p. 561. DOI: 10.1103/PhysRevLett.56.561.

[23] Y. Cai et al. "Front. Phys. 6, 40 (2018)". In: *Frontiers of Physics* 6 (2018), p. 40. DOI: 10.3389/fphy.2018.00040.

[24] S. Antusch et al. "JHEP 10, 84 (2006)". In: *Journal of High Energy Physics* 2006 (2006), p. 84. DOI: 10.1088/1126-6708/2006/10/084.

[25] Z. Liu, L.-T. Wang, and H. Zhang. In: *Chin. Phys. C* 41 (2017), p. 063102. DOI: 10.1088/1674-1137/41/6/063102.

[26] J. Liu et al. In: *Phys. Rev. D* 97 (2018), p. 095044. DOI: 10.1103/PhysRevD.97.095044.

[27] S. L. Glashow, J. Iliopoulos, and L. Maiani. "Weak Interactions with Lepton-Hadron Symmetry". In: *Phys. Rev. D* 2 (1970), p. 1285. DOI: 10.1103/PhysRevD.2.1285.

[28] G. Mann and T. Riemann. "Annihilation of e+e- Into Hadrons and QCD". In: *Ann. Phys.* 40 (1984), p. 334. DOI: 10.1016/0003-4916(84)90144-1.

[29] A. Abada et al. "Minimal Flavour Violation and Beyond for Leptogenesis in an $SO(10)_{\mathrm{GUT}}$ Framework". In: *JHEP* 4 (2015), p. 51. DOI: 10.1007/JHEP04(2015)051.

[30] M. Dam. *Tau physics at the FCC*. 15th Workshop on Tau Physics (2018). URL: https://indico.cern.ch/event/632562/.

[31] ALICE Collaboration and M. Mager. In: *Nuclear Instruments and Methods in Physics Research Section A* 824 (2016), p. 434. DOI: 10.1016/j.nima.2016.03.012.

[32] G. Chiarello et al. "A new construction technique of high granularity and high transparency drift chambers for modern high energy physics experiments". In: *Nuclear Instruments and Methods in Physics Research Section A: Accelerators, Spectrometers, Detectors and Associated Equipment* 824 (2016). Frontier Detectors for Frontier Physics: Proceedings of the 13th Pisa Meeting on Advanced Detectors, pp. 512–514. ISSN: 0168-9002. DOI: https://doi.org/10.1016/j.nima.2015.12.021. URL: https://www.sciencedirect.com/science/article/pii/S0168900215015922.

[33] A.M. Baldini et al. "MEG Upgrade Proposal". In: (2013). arXiv: arXiv:1301.7225[physics.ins-det]. URL: http://adsabs.harvard.edu/abs/2013arXiv1301.7225B.

[34] A.M. Baldini et al. "Investigation of Ultra-Low Background Conditions for NEXT". In: *JINST* 11 (2016), P07011. DOI: 10.1088/1748-0221/11/07/P07011.

[35] DREAM Collaboration and R. Wigmans. In: *Nuclear Instruments and Methods in Physics Research Section A* 617 (2010), p. 129.

[36] N. Akchurin et al. In: *Nuclear Instruments and Methods in Physics Research Section A* 735 (2014), p. 130.

[37] RD52 (DREAM) Collaboration and R. Wigmans. In: *Nuclear Instruments and Methods in Physics Research Section A* 824 (2016), p. 721.

[38] N. Akchurin et al. In: *Nuclear Instruments and Methods in Physics Research Section A* 735 (2014), p. 120.

[39] S. Braibant and P. Giacomelli. "Muon Detection at FCC-ee". In: *Eur. Phys. J. Plus* 136 (2021), p. 1143. DOI: 10.1140/epjp/s13360-021-02115-2. URL: https://doi.org/10.1140/epjp/s13360-021-02115-2.

[40] G. Bencivenni et al. "The μ-RWELL detector: a novel concept for large area, compact, resistive Micromegas". In: *JINST* 10 (2015), P02008. DOI: 10.1088/1748-0221/10/02/P02008.

[41] Fabio Sauli. "GEM: A new concept for electron amplification in gas detectors". In: *Nuclear Instruments and Methods in Physics Research Section A: Accelerators, Spectrometers, Detectors and Associated Equipment* 386 (1997), p. 531.

[42] R. Chechik et al. "Thick GEM-like multipliers—a simple solution for large area UV-RICH detectors". In: *Nuclear Instruments and Methods in Physics Research Section A: Accelerators, Spectrometers, Detectors and Associated Equipment* 553 (2005), p. 35.

[43] Y. Giomataris et al. "Micromegas: A high-granularity, position-sensitive gaseous detector for high particle flux environments". In: *Nuclear Instruments and Methods in Physics Research Section A: Accelerators, Spectrometers, Detectors and Associated Equipment* 376 (1996), p. 29.

[44] R. Santonico and R. Cardarelli. "Development of Resistive Plate Counters". In: *Nuclear Instruments and Methods in Physics Research Section A: Accelerators, Spectrometers, Detectors and Associated Equipment* 377 (1981), p. 187.

[45] D. Abbaneo et al. "GEM based detector for future upgrade of the CMS forward muon system". In: *Nucl. Instrum. Meth. A* 718 (2013), p. 383. DOI: 10.1016/j.nima.2013.05.029.

[46] G. Bencivenni et al. "Performance of μ-RWELL detector vs. resistivity of the resistive stage". In: *Nucl. Instrum. Meth. A* 886 (2018), p. 36. DOI: 10.1016/j.nima.2017.12.037.

[47] G. Bencivenni et al. "On the space resolution of the μ-RWELL". In: *JINST* 16 (2021), P08036. DOI: 10.1088/1748-0221/16/08/P08036.

[48] Stefano Gramigna. "TIGER/GEMROC: a Versatile and Modular Readout System for Micro-pattern Gaseous Detectors". In: *Proceedings of the 41st International Conference on High Energy Physics (ICHEP2022)*. on behalf of the CGEM-IT working group. Bologna, Italy, 2022.

[49] *Geant4, A Simulation Toolkit for Particle Transport and Detection*. https://geant4.web.cern.ch/.

[50] Elisa <1992> Fontanesi. "Precision measurements of the Higgs boson properties: from the H $\rightarrow$ ZZ* $\rightarrow$ 4l analysis with CMS at the LHC to the future large lepton colliders". PhD thesis. Bologna U., 2021. DOI: 10.6092/unibo/amsdottorato/9661.

[51] M. Frank et al. In: *J. Phys.: Conf. Ser.* 513 (2014), p. 022010.

[52] Markus Frank et al. *AIDASoft/DD4hep*. webpage: http://dd4hep.cern.ch/. Oct. 2018. DOI: 10.5281/zenodo.592244. URL: https://doi.org/10.5281/zenodo.592244.